Chemical processes in a young biomass-burning plume

Jörg Trentmann[1] and Meinrat O. Andreae

Biogeochemistry Department, Max Planck Institute for Chemistry, Mainz, Germany

Hans-F. Graf[2]

Max Planck Institute for Meteorology, Hamburg, Germany

[1] The photochemistry in young biomass-burning plumes depends on the emissions from the fire and their mixing with the background atmosphere as well as on the actinic flux. In the present study a three-dimensional plume model is used to investigate the photochemical evolution of a biomass-burning plume during the first tens of minutes after the fire emissions have been released into the atmosphere. The model results represent the evolution of the plume from the Quinault prescribed fire conducted during the Smoke, Cloud, and Radiation-C (SCAR-C) experiment. The modeled ozone concentrations of about 70 ppb are close to observations. The main nitrogen reservoir species downwind of the fire are HNO_3 and peroxyacetyl nitrate, accounting for about ~60% and ~30% of the total nitrogen reservoir species, respectively. Photolysis of formaldehyde, which is emitted from the fire, is the primary source of radicals in the plume. Omitting the emissions of oxygenated volatile organic compounds in the modeled fire plume leads to unrealistically low ozone concentrations in the simulations. A nonabsorbing aerosol as well as the lower emission of NO_x in the simulations enhance the radical concentration, the photochemical ozone formation, and the oxidation efficiency, at least at the timescales considered here. Further investigations of the atmospheric processes in young biomass-burning plumes will increase our understanding of the interaction of transport and chemical processes not only in biomass-burning plumes but also in other convective systems. *INDEX TERMS:* 0345 Atmospheric Composition and Structure: Pollution—urban and regional (0305); 0365 Atmospheric Composition and Structure: Troposphere—composition and chemistry; 0368 Atmospheric Composition and Structure: Troposphere—constituent transport and chemistry; 3329 Meteorology and Atmospheric Dynamics: Mesoscale meteorology; *KEYWORDS:* biomass burning, photochemistry, atmospheric modeling

1. Introduction

[2] Vegetation fires are a major source of several atmospheric trace gases as well as aerosol particles [*Crutzen and Andreae*, 1990; *Andreae and Merlet*, 2001]. Photochemical processing of the primary emissions leads to the formation of secondary pollutants, e.g., ozone. Several field studies have shown the influence of primary emissions from biomass burning on atmospheric composition and the formation of secondary pollutants in different regions, e.g., the Arctic [*Harriss et al.*, 1994], the South Atlantic [*Andreae et al.*, 1996a], Brazil [*Kaufman et al.*, 1998], and northern Africa [*Delmas et al.*, 1999]. Long-term satellite measure-

ments provide evidence that vegetation fires influence the atmospheric composition regularly on a regional to global scale, especially in the tropics [*Fishman et al.*, 1991; *Fishman and Brackett*, 1997; *Thompson et al.*, 2001; *Chandra et al.*, 2002; *Peters et al.*, 2002].

[3] Global atmospheric chemistry models that include emissions from biomass burning have been used to quantify the contribution of biomass-burning emissions to the atmospheric concentrations of several trace gases, e.g., CO, NO_x (NO_x = NO + NO_2), and O_3. The impact of biomass burning on the global tropospheric ozone concentration was investigated in several studies [e.g., *Lelieveld and Dentener*, 2000; *Marufu et al.*, 2000; *Galanter et al.*, 2000; *Granier et al.*, 2000]. All studies estimate the contribution of biomass burning to the global tropospheric ozone concentration to be in the order of 10%. Nevertheless, on a regional scale close to the source region, biomass burning contributes to a much larger extent to the ozone concentration [*Marufu et al.*, 2000; *McKeen et al.*, 2002].

---

[1]Now at Department of Atmospheric Sciences, University of Washington, Seattle, Washington, USA.

[2]Now at Department of Geography, University of Cambridge, Cambridge, UK.

[4] Several observations give evidence that photochemical ozone production takes place already in very young biomass-burning plumes, i.e., a few tens of minutes after the fire emissions are released [*Evans et al.*, 1977; *Stith et al.*, 1981; *Hobbs et al.*, 1996, 2003; *Goode et al.*, 2000; *Yokelson et al.*, 2003; *Jost et al.*, 2003]. The ozone production in individual biomass-burning plumes was found to be significant for the regional-scale ozone budget in the tropical South Atlantic region [*Mauzerall et al.*, 1998]. However, regional and global scale models cannot describe the ozone production in individual plumes, because of their coarse grid compared to the size of a biomass-burning plume. In these models, emissions from biomass burning are introduced and homogeneously distributed into a large area. This artificial dilution might lead to an overestimation or underestimation of the ozone concentration, depending on the concentrations and on the size of the model grid box [*Chatfield and Delany*, 1990; *Poppe et al.*, 1998].

[5] In order to study the chemical processes in biomass-burning plumes, box model studies have been performed [e.g., *Jacob et al.*, 1992; *Mauzerall et al.*, 1998; *Mason et al.*, 2001; *Jost et al.*, 2003]. For a realistic simulation, dilution of the emitted species has to be taken into account. The amount of dilution is a sensitive parameter in these simulations, because the amount of background air mixed into the fire-affected air parcel strongly influences the amount of ozone produced [*Chatfield and Delany*, 1990; *Poppe et al.*, 1998].

[6] In the present study, the chemical evolution as well as the transport of the biomass-burning emissions are considered in detail. The goal of this study is to investigate the chemical processes leading to the formation of ozone during the first tens of minutes after the fire emissions are released into the atmosphere. Understanding and quantifying these processes will help to improve the representation of vegetation fires in regional and global model studies. The framework for this study is the active tracer high-resolution atmospheric model (ATHAM) [*Herzog et al.*, 1998; *Oberhuber et al.*, 1998; *Graf et al.*, 1999]. ATHAM has been used previously to simulate the transport of aerosol particles from a prescribed fire, and the results showed reasonable agreement with measurements [*Trentmann et al.*, 2002]. Here, these dynamical simulations are extended to include chemical processes.

2. Model Description

[7] The three-dimensional (3-D) nonhydrostatic plume model ATHAM was designed and used originally for the study of volcanic plumes [*Graf et al.*, 1999]. (For a detailed description of the meteorological and microphysical modules of ATHAM, see *Oberhuber et al.* [1998], *Herzog et al.* [1998], and *Textor et al.* [2003].)

[8] ATHAM is formulated with a modular structure that allows the inclusion of independent modules. Existing modules treat the dynamics, turbulence, transport, cloud microphysics, gas scavenging, radiation, emissions, and chemistry. In the present investigation, only the transport, turbulence, radiation, emission, and chemistry modules of ATHAM are used. The transport of chemical species is based on a slightly modified version of the method of *Smolarkiewicz* [1984]. The turbulent quantities are calculated using a modified Kolmogorov-Prandtl formulation. The solar radiation is calculated with the 2-stream practical improved flux method (PIFM) [*Zdunkowski et al.*, 1982], including radiative effects of gases and aerosol particles. The chemical module is described in more detail in the following.

[9] Atmospheric chemistry in biomass-burning plumes is dominated by the gaseous emissions from the fire. These include CO and other volatile organic compounds (VOCs), nitrogen oxides, as well as halogen-containing and sulfur-containing compounds [*Andreae and Merlet*, 2001]. In order to describe the chemical processes in a three-dimensional transport model, a selection of species and reactions has to be performed due to computational limitations. The appropriate selection of the included species depends on the simulation time, the target species, as well as on the available computer resources. For our specific purpose, a selection of chemical reactions was performed to reproduce the chemical processes in a young biomass-burning plume that lead to the formation of ozone within the first tens of minutes after the release of the emissions into the atmosphere.

[10] Atmospheric chemistry occurring in young biomass-burning plumes is characterized by high concentrations of VOCs and nitrogen oxides. Photochemical ozone production in biomass-burning plumes is driven by the oxidation of VOCs by the hydroxy radical (OH) in the presence of high concentrations of NO_x. One substantial difference between urban and biomass-burning emissions is the large amount of oxygenated volatile organic compounds (OVOC) that are emitted by vegetation fires. The most important OVOCs emitted from biomass burning are aldehydes, e.g., HCHO, CH_3CHO, organic acids, e.g., HCOOH, CH_3COOH, alcohols, e.g., CH_3OH, and ketones, e.g., CH_3COCH_3.

[11] The chemical mechanism used in the present study includes the oxidation of the primary emissions from biomass burning: CO, CH_4, C_2H_6, C_2H_4, C_3H_6, HCHO, CH_3CHO, HCOOH, CH_3COOH, and CH_3COCH_3. Higher hydrocarbons are neglected because of their low emission ratios. Oxidation by OH is considered for all emitted species. Photolysis of aldehydes and acetone is included as well as ozonolysis of the alkenes. Oxidation of ethene is treated explicitly based on a recent laboratory study [*Orlando et al.*, 1998]. Because of the high NO_x concentrations, cross reactions between higher peroxy radicals are not important under the present conditions [*Kirchner and Stockwell*, 1996] and are not taken into account.

[12] Two heterogeneous reactions on aerosol particles are included in the mechanism: the reaction of NO_2 to yield HONO, and that of N_2O_5 to yield HNO_3. Heterogeneous reaction rates are calculated as first-order rate constants, $k_{het} = (1/4)\gamma cS$, where γ is the uptake coefficient, c the mean molecular speed, and S the aerosol surface per volume of air. The aerosol surface is calculated from the time-dependent aerosol mass concentration using a surface area per particle of 1.6×10^{-9} cm^2, derived from measurements of the aerosol size distribution [see *Gassó and Hegg*, 1998; *Trentmann et al.*, 2002].

[13] Photolysis frequencies, which include the effect of absorption and scattering by molecules and aerosol particles are calculated on-line [*Landgraf and Crutzen*, 1998] using the actinic flux calculated with PIFM2. The method of *Landgraf and Crutzen* [1998] requires precalculation of polynomial coefficients for the calculation of the photolysis

frequencies. For compounds for which these coefficients were not available, the photolysis frequencies were calculated from the linear correlation with a photolysis frequency of a compound with similar absorption cross section and quantum yield [*von Kuhlmann et al.*, 2003]. The complete reaction set is given in the appendix.[1]

[14] Simulated concentrations from this mechanism were compared to those from a more detailed chemical mechanism in photochemical box model studies [*Jost et al.*, 2003]. The agreement for simulations representing the first hours of a young biomass-burning plume was very good.

[15] The numerical solution of the differential equations for the chemical integration is performed using the kinetic preprocessor (KPP) [*Damian et al.*, 2002]. In the present work, a 2-stage Rosenbrock method (ROS2) was applied to solve the chemical differential equations [*Verwer et al.*, 1999].

3. Model Initialization

[16] In this study, ATHAM is used with a time-independent three-dimensional field of the meteorological quantities (wind, temperature, pressure) taken from the ATHAM simulation presented by *Trentmann et al.* [2002]. The scenario in this previous study was shown to give a reasonably good representation of the plume from the Quinault prescribed fire on 21 September 1994. This 19.4 ha clear-cut burn on the Pacific Coast of Washington State on the Olympic Peninsula and the resulting plume was intensively studied by remote sensing and in situ measurements during the Smoke, Cloud, and Radiation-C (SCAR-C) experiment [*Kaufman et al.*, 1996; *Hobbs et al.*, 1996; *Martins et al.*, 1996; *Tanré et al.*, 1997; *Gassó and Hegg*, 1998]. The simulated fields of the meteorological quantities were linearly interpolated on the new model grid and kept constant over the simulated time of 90 min. The wind field was interpolated in such a way to keep it free of divergence. The advantage of this strategy is that the model domain can be kept small, which significantly reduces the required computer power.

3.1. Model Setup

[17] The three-dimensional model domain (x, y, z) of ATHAM was set to 20 km $\times$ 7 km $\times$ 900 m with a minimal grid spacing of 50 $\times$ 50 $\times$ 30 m in the central part of the model domain. The number of grid boxes in the x direction, y direction, and z direction was 85, 66, and 25, respectively. The transport timestep was set to 3 s. Two chemical time steps of 0.6 s and 2.4 s were calculated during one transport time step. The solar zenith angle was computed for 47°N, 21 September, representing the conditions during the Quinault fire. Model simulations were set to correspond to an ignition at 1100 LT and duration of 90 min.

3.2. Initial Conditions

[18] Three-dimensional temperature and wind fields from the previous simulation of the Quinault fire [*Trentmann et al.*, 2002] representing the situation 90 min after ignition are used in the present study. The atmospheric conditions

Table 1. Initial Surface Mixing Ratios for the Chemical Compounds

Species	Mixing Ratio, ppt
O_3	28.8[a]
CO	154[a]
CH_4	1.82[b]
C_2H_6	800
C_2H_4	500
C_3H_6	100
CH_3OH	3.6[a]
CH_3COCH_3	2.7[a]
HCHO	1.6[a]
CH_3CHO	300
HCOOH	68
CH_3COOH	78
H_2O_2	400
CH_3OOH	300
NO_x	3.6[a]
HNO_3	500
PAN	400

[a]Given in ppb.
[b]Given in ppm.

are determined by a strong temperature inversion between ~300 m and 600 m that prevents the fire-induced convection from reaching higher altitudes. The fire emissions are transported with the horizontal wind of ~3.5 m s^{-1}.

[19] Initial vertical profiles for the background chemical species are taken from the model of atmospheric transport and chemistry (MATCH) [*Lawrence et al.*, 1999; *von Kuhlmann et al.*, 2003]. Monthly mean values for September at 47°N, 124°W were used. The initial surface values of the relevant chemical species are given in Table 1. Ozone mixing ratios in the range of 30 ppb are comparable to observations during the Quinault fire [*Hobbs et al.*, 1996]. While the ozone concentration slightly increases with altitude, the carbon monoxide, NO_x, and VOC concentrations decrease with increasing altitude.

3.3. Fire Emissions

[20] Time-dependent fire emissions for the Quinault fire were obtained from the emission production model (EPM) [*Sandberg and Peterson*, 1984; *Ferguson et al.*, 2000]. The EPM simulations have been initialized with the observed loading and moisture of different fuel size classes and the duff from the Quinault fire site [*Hobbs et al.*, 1996]. EPM simulates the time-dependent emissions of energy, particulate matter, CO_2, CO, and CH_4, accounting for different phases of the fire (flaming and smoldering). The use of these heat and particulate emissions resulted in reasonable agreement between results from the simulation of the particulate transport and observations from the Quinault fire plume [*Trentmann et al.*, 2002]. In this study, the CO_2, CO, CH_4, and aerosol emissions are taken from the EPM. As no detailed information on the emissions from the Quinault fire is available, the emissions of the other trace gases are calculated using the emission factors presented in Table 2.

[21] Measurements of the initial NO/NO_x ratio are very sparse; most of them point to values slightly less than 90% [*Griffith et al.*, 1991; *Delmas et al.*, 1995; *Yokelson et al.*, 1996]. Theoretical considerations indicate that in the smoldering stage the NO/NO_x ratio can decrease to 60% [*Lobert*

---

[1]Auxiliary material is available at ftp://ftp.agu.org/apend/jd/2003JD003732.

Table 2. Emission Ratios Related to CO for the Trace Gases Emitted by Vegetation Fires Used in the Present Study

Compound	$\Delta X/\Delta CO$, %	Notes[a]
Acetic acid (CH_3COOH)	2.0	2
Formaldehyde (HCHO)	2.0	3
Ethene (C_2H_4)	1.2	1
Acetaldehyde (CH_3CHO)	1.2	4
Methanol (CH_3OH)	1.0	3
Formic acid (HCOOH)	0.9	5
Ethane (C_2H_6)	0.7	1
Acetone (CH_3COCH_3)	0.5	4
Propene (C_3H_6)	0.5	1
Nitrogen oxides (NO_x)[b]	0.2	1

[a]1, emission ratio taken from *Lobert et al.* [1991]; 2, emission ratio derived from *Yokelson et al.* [1997] and *Goode et al.* [1999]; 3, emission ratio derived from *Yokelson et al.* [1997], *Holzinger et al.* [1999], and *Goode et al.* [1999]; 4, emission ratio taken from *Holzinger et al.* [1999]; 5, emission ratio taken from *Yokelson et al.* [1997].

[b]For NO_x the emission ratio related to CO_2 is given.

and Warnatz, 1993]. In the following simulations, a value of 75% for the NO/NO_x ratio is used. The temporal and spatial distribution of the fire emissions is identical to the one used in *Trentmann et al.* [2002].

3.4. Calculation of the Photolysis Frequencies

[22] For the calculation of the photolysis frequencies, the vertical extent of the model domain is increased up to 60 km. Inside the ATHAM model domain, i.e., up to an altitude of 900 m, temperature, pressure, as well as ozone and aerosol concentrations, are taken from the simulations. Above 900 m, observations, supplemented by data from the standard atmosphere for midlatitude summer conditions, are used as described in *Trentmann et al.* [2002]. No aerosol is considered above 900 m. The wavelength-independent surface albedo was assumed to be Lambertian and set to 6%.

[23] The interaction of the smoke particles with the solar radiation is included in the calculation of the photolysis frequencies. The aerosol optical properties were calculated on the basis of measurements of the aerosol composition [*Martins et al.*, 1996] and size distribution [*Hobbs et al.*, 1996; *Gassó and Hegg*, 1998] from the Quinault fire as explained in our previous study [*Trentmann et al.*, 2002]. The optical properties of the aerosol are linearly interpolated on the wavelength grid used for the calculation of the photolysis frequencies [*Landgraf and Crutzen*, 1998]. Photolysis frequencies were calculated at every transport time step in order to account for the changing spatial distribution of the aerosol.

[24] One-dimensional radiative transfer simulations were performed for every column of the model (independent pixel approximation (IPA) [*Cahalan et al.*, 1994]). No interaction between neighboring columns was considered, i.e., no horizontal photon transfer. The neglect of three-dimensional radiation effects has a significant impact on the calculated photolysis frequencies, especially in the center of the plume above the fire [*Trentmann et al.*, 2003]. However, 3-D radiative transfer simulations cannot be performed on-line within a 3-D atmospheric transport model at the present, because of computational limitations. Nevertheless, their possible effects should be kept in mind when interpreting the model results.

[25] In the following sections, we will first present the results from the reference (REF) simulation as described above. In section 5, the results from three sensitivity studies will be presented and compared to the results from the reference simulation.

4. Model Results

[26] The general appearance of the biomass-burning plume is characterized by the concentration of passive tracers. The term "passive" is used here to indicate that the atmospheric concentrations of these trace species are not significantly influenced by photochemistry on the timescale considered here. Their spatial distribution is identical in all model simulations, because their concentrations are only influenced by transport effects.

[27] In the following analysis, the extent of the plume is defined by the aerosol mass concentration. Every grid cell with an aerosol mass concentration exceeding the threshold of $10\,\mu g\,m^{-3}$ is considered to be in the plume. Only those grid cells are considered when plume-averaged quantities are presented.

4.1. Passive Tracers

[28] As tracer transport in this study is performed with a constant wind field, the resulting spatial distribution of the passive tracers from the fire differs slightly from the simulation presented in *Trentmann et al.* [2002].

[29] In Figure 1a, the simulated aerosol optical depth τ at 400 nm after 90 min is shown. Above the fire, τ exceeds 10; downwind it decreases to values between 0.2 and 1. Figure 1b shows the CO mixing ratio along the main plume axis, depicted as section A in Figure 1a. Figure 1c presents the CO mixing ratio along section B, and Figure 1d shows the values of the CO mixing ratio at an altitude of 500 m. CO and aerosol particles are emitted from the fire and transported up to an altitude of $\sim$700 m. The horizontal transport takes place at altitudes between 350 m and 600 m in the planetary boundary layer. The maximum traveling distance within the 90-min simulation time is around 16 km. The simulated CO mixing ratio in the plume is much higher than the background mixing ratio. At a distance of 8.2 km from the fire, corresponding to a traveling time of $\sim$40 min, the maximum and the average mixing ratio of CO in the plume are 5.9 ppm and 1.2 ppm, respectively.

[30] The average mixing ratios at the source, defined as the horizontal average at an altitude of 150 m above the fire, as well as the average mixing ratios across the plume at a distance of 8.2 km, section B in Figure 1a, for all compounds emitted by the fire are presented in Table 3.

[31] The high concentrations of VOCs and NO_x in Table 3 as compared to the background concentrations (Table 1) demonstrate the strong impact of the fire on the chemical composition. The concentrations downwind the fire are smaller than those close to the fire, because of the mixing of the plume with background air and the increasing fire emissions as a function of time. Additionally, chemical processing influences the concentration of the nonpassive species during the simulation time of 90 min.

[32] In our previous study, we showed that the simulated aerosol mass concentration compares well with observations [*Trentmann et al.*, 2002]. No CO measurements from the
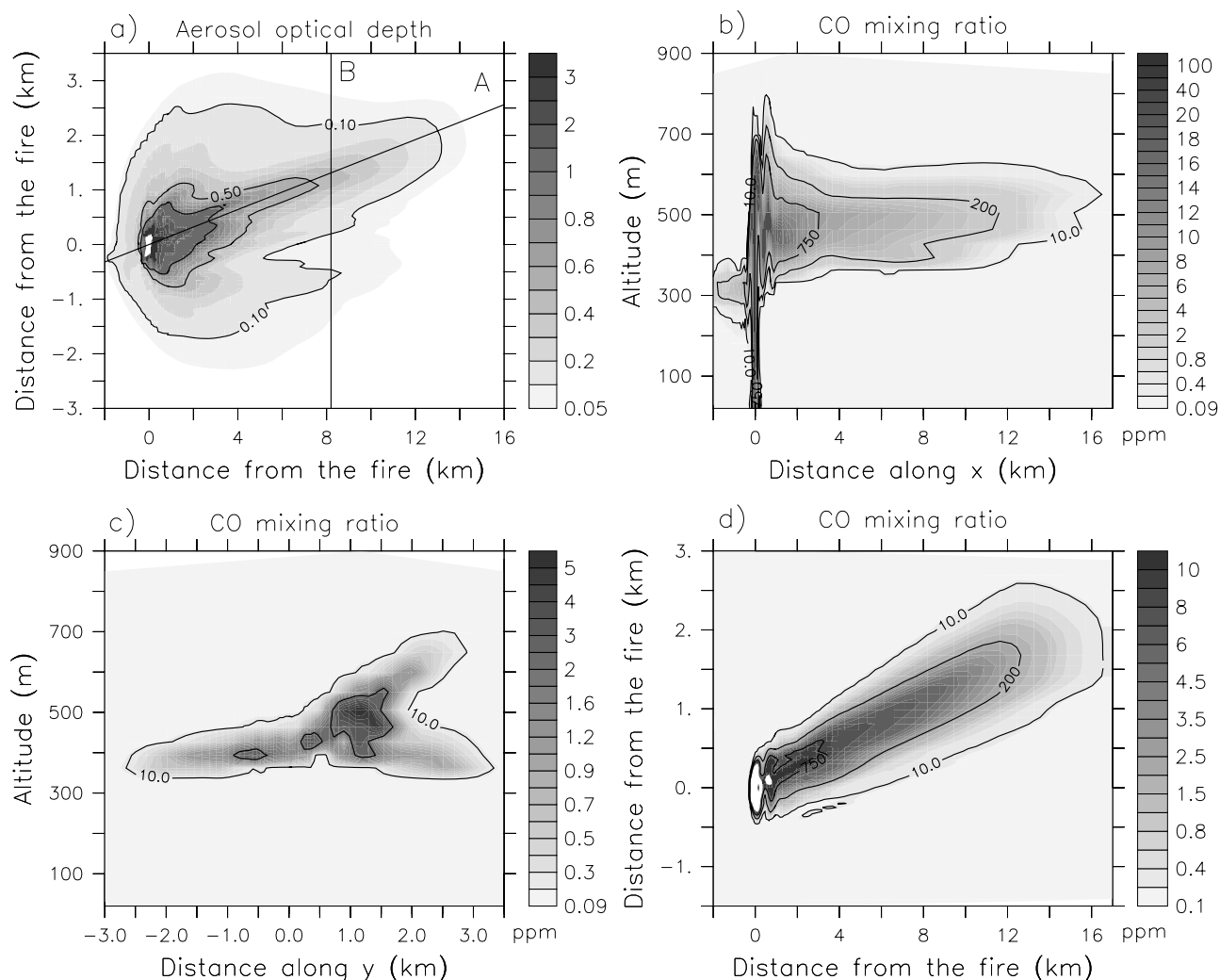
Figure 1. (a) Aerosol optical depth at 400 nm (color coding) after 90 min of simulation. The locations of the cross sections A and B are also shown. (b) CO mixing ratio (color coding) along the main plume axis, section A. (c) CO mixing ratio at section B across the plume at $x = 8.2$ km. (d) CO mixing ratio at an altitude of $z = 500$ m. Contour lines in Figures 1b–1d represent the aerosol mass concentration ($\mu g\ m^{-3}$). The white line indicates the border of the plume as defined by an aerosol mass concentration of 10 $\mu g\ m^{-3}$. See color version of this figure at back of this issue.

Quinault fire are available for a comparison and evaluation of the model results. However, other investigations of young biomass-burning plumes found CO concentrations comparable to the simulated values [e.g., *Ward et al.*, 1992; *Andreae et al.*, 1996b; *Koppmann et al.*, 1997; *Ferek et al.*, 1998; *Goode et al.*, 2000]. This reasonable agreement between observed and simulated CO mixing ratios makes us confident that the simulated gas phase concentrations are representative for the conditions in young biomass-burning plumes. Therefore the simulation of the photochemical processes that are closely linked to the concentrations of VOC and NO_x should be a reasonably realistic representation of the photochemical processes occurring in young biomass-burning plumes.

4.2. Photochemical Processes in a Biomass-Burning Plume

[33] In the following sections, results from the REF simulation for several trace gases are presented and compared to

Table 3. Source and Downwind Mixing Ratio of the Emitted Trace Gases[a]

Species	Mixing Ratio, ppb	
	Fire	Downwind
CO	18000	1200
CH_4	2818	1877
C_2H_6	125.9	8.0
C_2H_4	214.9	11.3
C_3H_6	89.3	3.3
CH_3COCH_3	92.0	7.2
HCHO	359.2	21.9
CH_3CHO	214.8	11.9
CH_3OH	182.2	12.8
HCOOH	161.0	9.4
CH_3COOH	357.7	20.7
NO_x	403.9	22.2

[a]The mixing ratio close to the fire is calculated as the average plume mixing ratio at $z = 150$ m. The downwind average is for the cross section at $x = 8.2$ km, also shown in Figure 1c.
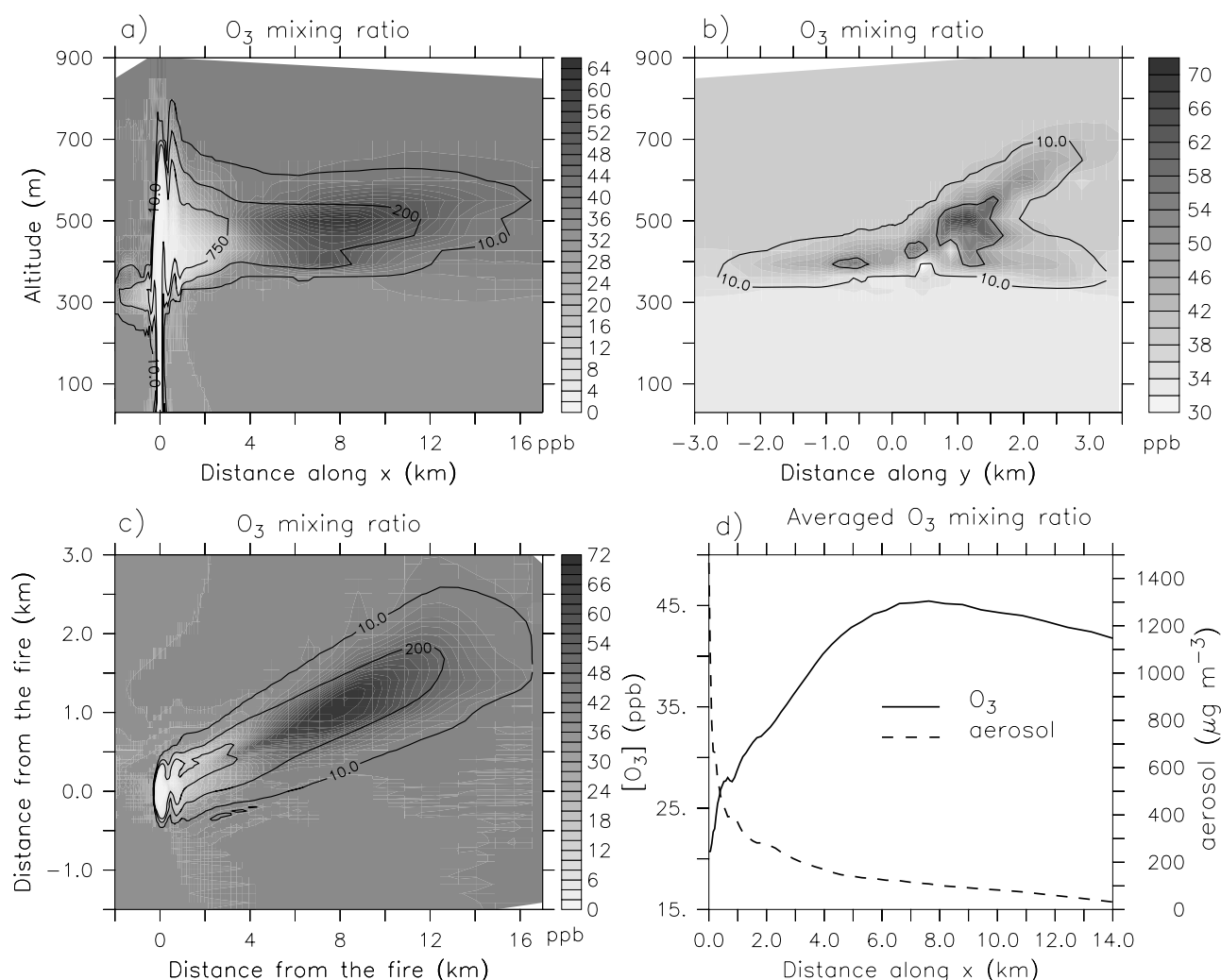
Figure 2. O_3 mixing ratio (color coding) for three cross sections through the model domain at (a) the main plume axis, section A in Figure 1a, (b) $x = 8.2$ km, section B in Figure 1a, and (c) $z = 500$ m after 90 min of simulation time. The traveling time from the source to the cross section at a distance of 8.2 km is ~40 min. Contour lines represent the aerosol mass concentration (μg m^{-3}). (d) Plume-averaged O_3 mixing ratio and aerosol mass concentration with distance from the fire. See color version of this figure at back of this issue.

appropriate measurements. The focus is on compounds that are altered by chemical processes in the biomass-burning plume. In particular, the production of ozone and the formation of nitrogen reservoir species are investigated. Additionally, the oxidation efficiency in the plume is examined.

[34] To distinguish between dynamical and chemical processes, correlations between chemical compounds are regularly used in the analysis of measurements of plumes from biomass burning or other sources [e.g., *Andreae et al.*, 1988, 1994, 2001; *Parrish et al.*, 1993; *Mauzerall et al.*, 1996, 1998; *Reid et al.*, 1998; *Ryerson et al.*, 1998; *Goode et al.*, 2000]. In these analyses, simultaneous measurements of the mixing ratios of two compounds, X and Y, are subjected to a linear regression analysis. The slope of the regression line ($\Delta X/\Delta Y$) is the so-called enhancement ratio within the polluted air mass relative to the background. In the present model study, the enhancement ratio between two species is calculated in the same way and can be compared to analyses based on observational data.

[35] From model simulations, photochemical reaction rates can be extracted. Two different quantities are used in the following sections. Spatially averaged and temporally averaged chemical reaction rates (molecule cm^{-3} s^{-1}) in the plume as well as temporally and spatially integrated rates are presented. The integrated rate gives the total number of molecules produced or destroyed by a specific chemical reaction in the plume during the simulation time of 90 min. From this quantity, the photochemical lifetime of a compound is derived by dividing its total emissions by its integrated chemical loss.

4.2.1. Ozone

[36] In this section, the simulated ozone concentration, the enhancement ratio of ozone compared to CO, and the photochemical processes leading to the production of ozone are presented. In Figure 2, the simulated ozone mixing ratio after 90 min is shown for one cross section along the main plume axis (Figure 2a, section A in Figure 1a), one cross section across the plume (Figure 2b,
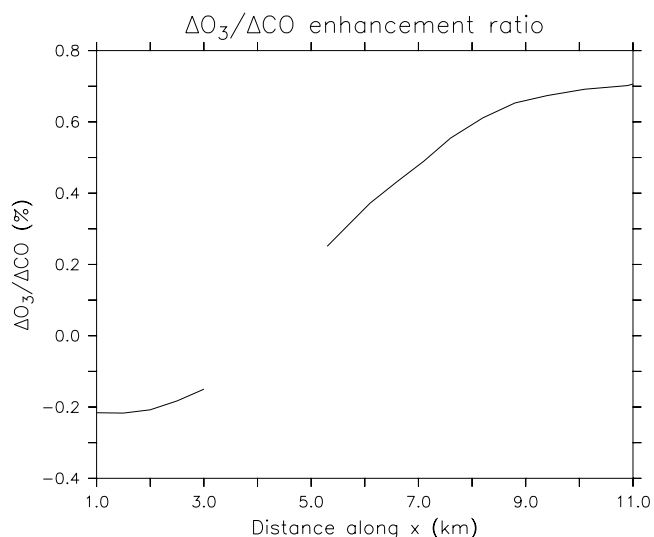
Figure 3. Evolution of the $\Delta O_3/\Delta CO$ ratio as a function of distance from the fire for the REF simulation. For the linear regression analysis, only grid cells between 300 m and 800 m altitude were taken into account. Only enhancement ratios with $R^2 > 0.6$ are displayed.

section B in Figure 1a) and one cross section at an altitude of 500 m (Figure 2c).

[37] Above the fire, ozone is strongly depleted due to the fast reaction of ozone with NO, which is emitted from the fire. The NO_x mixing ratio above the fire exceeds the background O_3 mixing ratio (compare Table 1 and Table 3), resulting in a complete titration of the available ozone into NO_2. Downwind of the fire, the ozone concentration gradually increases due to photochemical processes. In Figure 2b, the simulated ozone mixing ratio across the plume after $\sim$40 min of traveling is presented. The ozone concentrations within the plume are well above background level, with the maximum values being correlated with the highest aerosol concentrations.

[38] Figure 2d shows the plume-averaged ozone mixing ratio along the plume, together with the plume-averaged aerosol mass concentration. The aerosol concentrations gradually decrease with distance, while the averaged ozone concentration along the plume increases up to a value of 45 ppb, because of photochemical processes that lead to photochemical ozone production. The maximum and the averaged simulated ozone mixing ratio within the plume are 70 ppb and 40 ppb, respectively.

[39] The $\Delta O_3/\Delta CO$ enhancement ratio as a function of distance from the fire is presented in Figure 3. Close to the fire, ozone and CO are anticorrelated. With increasing distance from the fire, the $\Delta O_3/\Delta CO$ enhancement ratio increases, indicating photochemical ozone production during the transport of the emissions. At a distance of 12 km from the fire, the enhancement ratio is 0.75%. Between 3 and 5 km, no linear correlation was found between CO and ozone.

[40] Measurements in young biomass-burning plumes regularly show reduced ozone concentrations close to the fire and enhanced ozone concentrations downwind the fire. Observations during the Quinault fire revealed a minimum ozone mixing ratio of $\sim$5 ppb above the fire, and a maximum of $\sim$80 ppb downwind the fire [see *Hobbs et al.*, 1996, Figure 66.14]. Downwind ozone concentrations between 60 ppb and $\sim$150 ppb were also observed in other comparable biomass-burning plumes [*Evans et al.*, 1977; *Stith et al.*, 1981; *Goode et al.*, 2000; *Jost et al.*, 2003; *Hobbs et al.*, 2003; *Yokelson et al.*, 2003]. The simulated ozone concentration in the REF simulation therefore seems to be a good representation of the ozone concentration in young biomass-burning plumes.

[41] Measurements of the $\Delta O_3/\Delta CO$ enhancement ratios in Africa yielded values ranging from 1.2% to 16% with an average of 4% for biomass-burning plumes a few hours after emission [*Helas et al.*, 1995]. A $\Delta O_3/\Delta CO$ enhancement ratio of 15 ± 37% was derived from measurements within four fresh plumes (less than half a day old) observed during the Transport and Atmospheric Chemistry Near the Equator-Atlantic (TRACE-A) expedition [*Mauzerall et al.*, 1998]. The relatively large standard variation indicates that at least in one plume a significantly lower enhancement ratio than the average was observed. A $\Delta O_3/\Delta CO$ enhancement ratio of 7.9 ± 2.4% was derived from measurements within an Alaskan biomass-burning plume $\sim$2 h traveling time downwind the fire [*Goode et al.*, 2000]. Within a second plume, no correlation between CO and O_3 was found. Recently, ozone enhancement ratios of several African fires have been determined, resulting in a value of about 10% between 40 min and 2 hours after the emission [*Jost et al.*, 2003; *Hobbs et al.*, 2003; *Yokelson et al.*, 2003]. The simulated value of the $\Delta O_3/\Delta CO$ enhancement ratio for the Quinault plume presented here ($\Delta O_3/\Delta CO = 0.75\%$), is at the lower end of the range of reported values. However, especially given the large variability in the observations, it appears still reasonable.

[42] In order to quantify the simulated photochemical ozone production, the rates of the chemical reactions are analyzed. Ozone itself is produced and destroyed in numerous chemical reactions. Most of them are part of null cycles, without net production or destruction of ozone. In order to exclude these null cycles from budget analysis, the odd oxygen family, O_x, is often introduced in photochemical studies [e.g., *Crutzen et al.*, 1999]. The odd oxygen family includes all chemical compounds that are converted to ozone in fast chemical reactions. Production of the O_x family, $P(O_x)$, is therefore equivalent to ozone production. In the present study, the odd oxygen family is defined as $O_x = O_3 + O(^1D) + O(^3P) + NO_2 + 2 NO_3 + 3 N_2O_5 + HNO_3 + HNO_4 +$ peroxyacetyl nitrate (PAN) $+ CH_3O_2NO_2$.

[43] Photochemical O_x production is dominated by the reactions of peroxy radicals, e.g., HO_2, with NO leading to the formation of NO_2 that is included in the O_x family. This reaction accounts for about 69% of the total photochemical ozone production. Besides the hydroperoxy radical, HO_2, the methylperoxy radical, CH_3O_2 (10%), the peroxyacetyl radical, PA (7%), the hydroxyethylperoxy radical, EO2 (6%), and the hydroxypropylperoxy radical, PO2 (8%), contribute to ozone production. The contribution of the peroxy radicals from the alkenes, i.e., EO_2 and PO_2, to the total O_x production exceeds the contribution of the methylperoxy radical, CH_3O_2. In the background atmosphere, only HO_2 and CH_3O_2 contribute significantly to the photochemical production of O_x [*Crutzen et al.*, 1999]. The average rate of O_x production within the plume for the
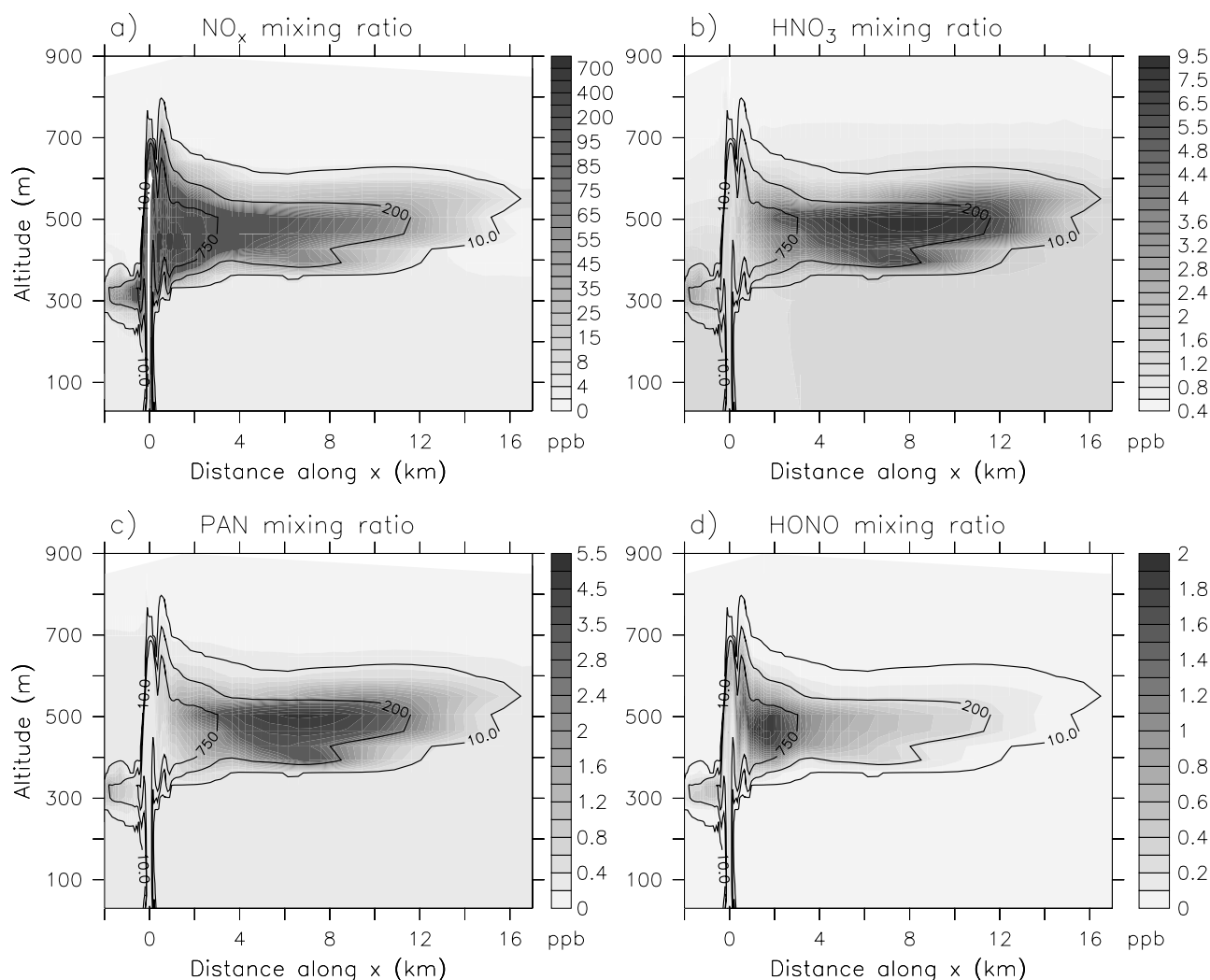
Figure 4. Mixing ratios of (a) NO_x and the most abundant NO_z species, i.e., (b) HNO_3, (c) PAN, and (d) HONO, along the main plume axis, section A in Figure 1a, after 90 min. Contour lines represent the aerosol mass concentration ($\mu g \ m^{-3}$). See color version of this figure at back of this issue.

90 min simulation is 1.84×10^8 molecule $cm^{-3} \ s^{-1}$ or ~ 25 ppb h^{-1}. The total number of photochemically produced O_x molecules in the plume during the 90 min is 5.67×10^{27}. During the same time, 1.32×10^{28} molecules of NO_x are emitted from the fire, yielding a photochemical production of 0.44 O_x per emitted NO_x after 90 min.

4.2.2. Nitrogen Species

[44] In Figure 4, the simulated mixing ratios of NO_x (Figure 4a) as well as the most abundant NO_z (NO_z = HNO_3 + HNO_4 + HONO + PAN + $CH_3O_2NO_2$) species, i.e., HNO_3 (Figure 4b), PAN (Figure 4c), and HONO (Figure 4d), are shown for the cross section along the plume (section A in Figure 1a). The NO_x concentration highly exceeds the NO_z concentration, and the photochemical formation of NO_z reduces the NO_x concentrations only slightly. As the nitrogen reservoir compounds are not emitted from the fire, their concentrations increase downwind of the fire due to photochemical production in the plume.

[45] The maximum HONO concentration occurs closer to the fire than the maximum mixing ratios of HNO_3 and PAN (Figure 4). Production of HONO mainly occurs via the reaction of NO with OH ($\sim 97\%$ of the total HONO

production) while photolysis is the main loss process of HONO. Close to the fire, the [NO]/[NO_2] ratio is larger than one, because of the high initial ratio from the fire emission. Downwind of the fire, this ratio decreases and production of HONO is reduced. Additionally, destruction of HONO due to photolysis increases downwind due to the lower aerosol optical depth. As the production of HNO_3 and PAN requires NO_2, their photochemical production increases downwind relative to the production of HONO. While PAN establishes a thermal equilibrium with NO_2, the loss of HNO_3 is dominated by reaction with OH. This reaction is slow on the timescale considered and leads to high HNO_3 concentrations.

[46] Figure 5a shows the plume-averaged NO_x and NO_z mixing ratios as a function of distance from the fire. The maximum and average mixing ratios of NO_z in the plume after 90 min of simulation are 19.3 ppb and 4.1 ppb, respectively. The most abundant NO_z compound is HNO_3 with a simulated maximum mixing ratio of 12.3 ppb. The maximum mixing ratios of PAN, HONO, HNO_4, and $CH_3O_2NO_2$ are 6.4 ppb, 2.4 ppb, 326 ppt, and 6.5 ppt, respectively.
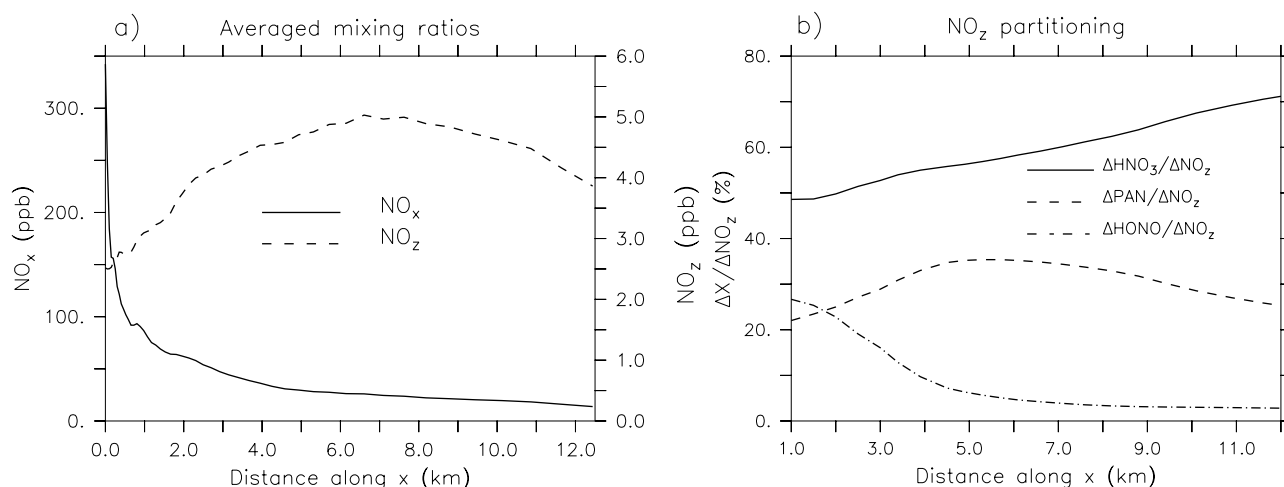
Figure 5. (a) Plume-averaged mixing ratio of NO_x and NO_z with distance from the fire after 90 min of simulation. (b) Partitioning of NO_z with distance from the fire, derived from linear correlations of HNO_3, PAN, and HONO with NO_z, respectively.

[47] Figure 5b presents the enhancement ratios between the dominant NO_z reservoir species, HNO_3, PAN, and HONO, as a function of distance from the fire. The contribution of HNO_3 to the total NO_z increases from roughly 50% close to the fire, to around 70% at 12 km. PAN contributes between 25% and 35% to the total NO_z. The contribution of HONO decreases with increasing distance from around 25% at 1 km to less than 5% at a distance of 6 km. The contribution of NO_z to the sum of all nitrogen species, NO_y ($NO_y = NO_x + NO_z$), increases steadily with distance from the fire reaching a value of 16% at 12 km downwind of the fire.

[48] Observations of the NO_x mixing ratios within the plume from the Quinault fire were in the order of a few hundred ppb close to the fire, and decreased with distance from the fire to values well below 10 ppb [*Hobbs et al.*, 1996]. The corresponding simulated values compare reasonably well with these observations. Observations within biomass-burning plumes from other fires yielded NO mixing ratios between ∼50 ppb and 260 ppb [*Evans et al.*, 1977; *Stith et al.*, 1981; *Griffith et al.*, 1991; *Goode et al.*, 2000; *Hobbs et al.*, 2003; *Yokelson et al.*, 2003], comparable to the values from the Quinault fire. Therefore we are confident that the simulated NO_x mixing ratios within the young plume are reasonably realistic.

[49] Measurements of HNO_3, PAN, or other compounds of the NO_z family in young biomass-burning plumes are rare. Observations in plumes from three prescribed fires yielded mean mixing ratios for HNO_3 of 14.6 ± 14.7 ppb, 40.7 ± 34.1 ppb, and 44.6 ± 33.1 ppb, respectively [*LeBel et al.*, 1988, 1991], larger than the simulated maximum mixing ratio of 12.3 ppb. During the Arctic Boundary Layer Experiment (ABLE-3B), a young biomass-burning plume was found with mixing ratios of HNO_3 and PAN of ∼700 ppt and ∼300 ppt, respectively, at low altitude [*Lefer et al.*, 1994; *Singh et al.*, 1994]. Although the simulated mixing ratios are larger than these observations, the measured HNO_3/PAN ratio of around 2.2 agrees fairly well with the modeled value of 1.9. From measurements performed between 1 km and 4 km altitude during TRACE-A, a

HNO_3/PAN ratio of 0.3 for "fresh plumes" (younger than 12 hours) was calculated [*Mauzerall et al.*, 1998], lower than in the simulations. However, these observations might not be suitable for a comparison as they were performed at higher altitudes.

[50] From the model simulations, the following values for the photochemical production of NO_z can be derived. The average net production rate of NO_z, i.e., $P(NO_z) - L(NO_z)$, in the plume is 2.82×10^7 molecule cm^{-3} s^{-1}. In total, 8.42×10^{26} molecules of NO_z were photochemically net produced within the plume during the simulation time of 90 min, with contributions from HNO_3, PAN, and HONO of 61%, 29%, and 7%, respectively. Together with the number of photochemically produced O_x molecules presented in section 4.2.1, the number of O_x molecules produced per number of NO_x molecules oxidized, i.e., per number of NO_z molecules formed, is calculated to 6.7. This value corresponds to the ozone production efficiency (OPE) that describes the number of produced ozone molecules per number of produced NO_z molecules [*Liu et al.*, 1987; *Trainer et al.*, 2000; *Marion et al.*, 2001]. The value of 6.7 is on the lower limit of the values reported from observations within the planetary boundary layer over Central Africa during the burning season (6.3 to 14.8) [*Marion et al.*, 2001]. The simulated lifetime of NO_x with respect to the formation of HNO_3 and PAN is 9.9 h.

4.2.3. Oxidizing Efficiency

[51] In Figure 6 the mixing ratios of OH (Figure 6a), HO_2 (Figure 6b), CH_3O_2 (Figure 6c), and the sum of other peroxy radicals, RO_2 (Figure 6d), along the plume are presented after a simulation time of 90 min. The concentration of RO_2 is dominated by the peroxy radicals from ethene and propene, EO_2 and PO_2, respectively. Above the fire, the concentrations of all radicals are close to zero. Downwind, the OH, HO_2, and CH_3O_2 concentrations in the plume are smaller than outside the plume, whereas the RO_2 concentration reaches its maximum value inside the plume. High NO_x concentrations are responsible for the enhanced photochemical removal of the radicals inside the plume, leading to the formation of several ppb of HNO_3, PAN, and
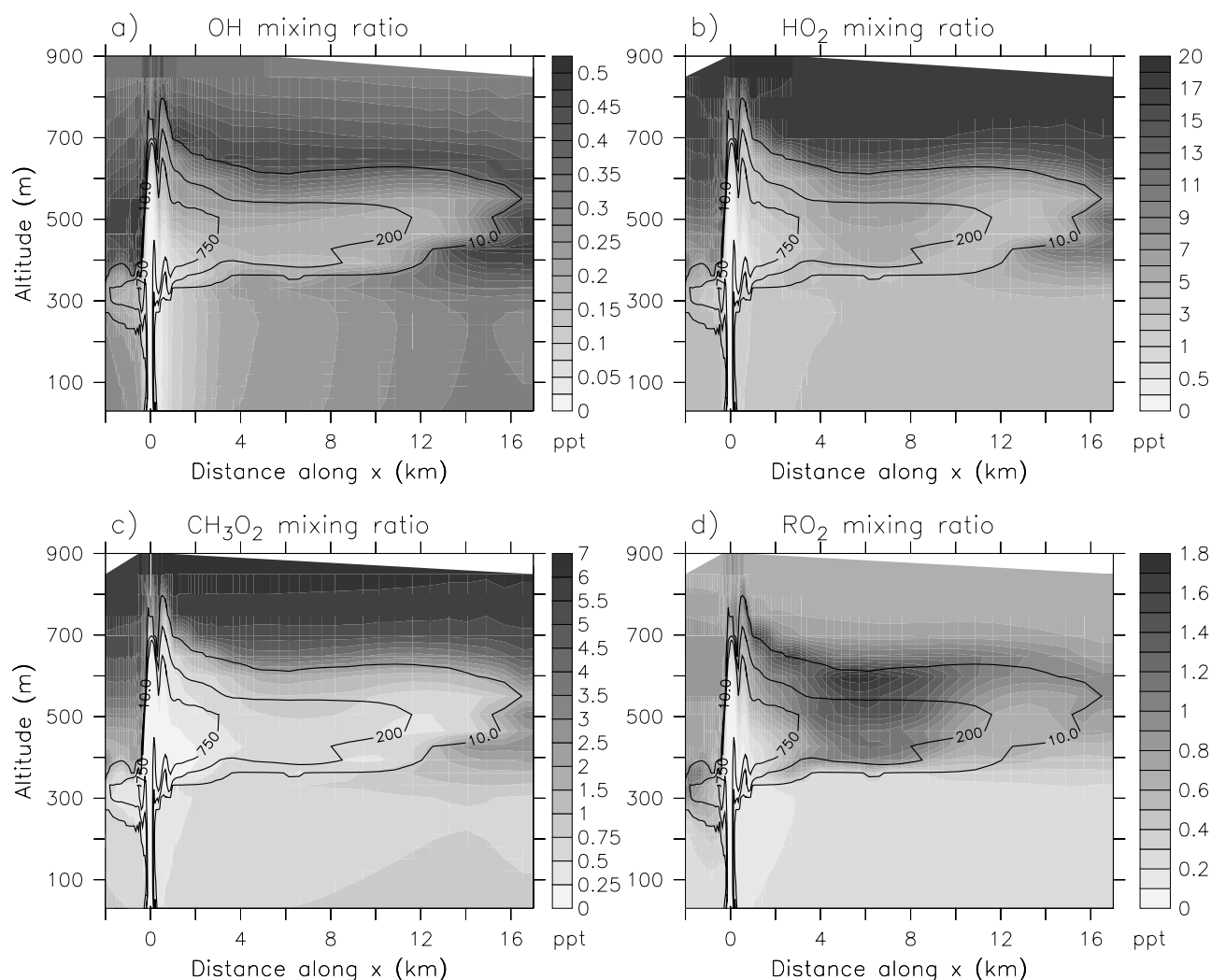
Figure 6. Simulated mixing ratios of (a) OH, (b) HO$_2$, (c) CH$_3$O$_2$, and (d) the sum of other peroxy radicals RO$_2$ (RO$_2$ = PA + C$_2$H$_6$O$_2$ + EO$_2$ + PO$_2$+ ACETO$_2$) after 90 min along the plume at $y = 100$ m. Contour lines represent the aerosol mass concentration (μg m^{-3}). See color version of this figure at back of this issue.

HONO (Figure 4). In the cases of OH, HO$_2$, and CH$_3$O$_2$, these enhanced losses compared to the background cannot be compensated by enhanced production. However, in the case of RO$_2$, the concentrations of the precursors, i.e., mainly ethene and propene, are highly elevated inside the plume. Additional photochemical production of RO$_2$ overcomes the enhanced photochemical destruction, and results in maximum concentrations of RO$_2$ inside the plume. The average mixing ratios of OH and HO$_2$ inside the plume after 90 min are 0.24 ppt and 4.92 ppt, respectively.

[52] In order to characterize the oxidation capacity, which is a quantity to describe the amount of atmospheric photochemical oxidation, we calculate enhancement ratios between alkenes and CO. In contrast to CO, the alkenes have a lifetime against reaction with OH that is comparable to the timescale considered here [*Jenkin and Clemitshaw*, 2000], and significant oxidation of alkenes occurs within the plume. This decreases the enhancement ratio of the alkenes against CO.

[53] In Figure 7, the enhancement ratios between propene and CO, and ethene and CO are presented. ΔC$_2$H$_4$/ΔCO

and ΔC$_3$H$_6$/ΔCO decrease almost linearly with increasing distance from the fire. This change in the enhancement ratio represents the different reactivities of the alkenes against OH oxidation as compared to CO and can be used as a measure for the oxidation efficiency in the plume.

[54] Observations during SCAR-B yielded a ΔC$_3$H$_6$/ΔCO enhancement ratio of 0.39% in young smoke plumes (less than 4 min after emission) [*Reid et al.*, 1998]. For measurements in aged regional haze, this ratio decreased to a value of 0.028% [*Reid et al.*, 1998]. During TRACE-A, the ΔC$_3$H$_6$/ΔCO enhancement ratio could only be determined for fresh plumes (0.12%). In recent (<1 day old) plumes, however, no correlation between propene and CO was found [*Mauzerall et al.*, 1998]. For ethene, the enhancement ratio compared to CO decreased from 0.69% in fresh plumes to 0.13% in recent plumes. In more aged biomass-burning plumes, no correlation between ethene and CO was found. From measurements in a young Alaskan biomass-burning plume, a slight reduction of ΔC$_2$H$_4$/ΔCO from an initial value of 1.9% to a value of 1.6 ± 0.2% after ~2.2 hours of traveling was observed [*Goode et al.*, 2000].
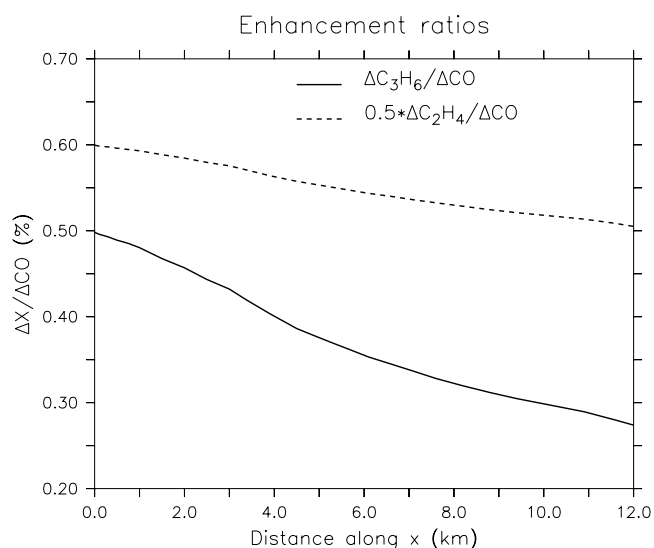
Figure 7. Enhancement ratios between C_2H_4 and CO and between C_3H_6 and CO as a function of distance from the fire after 90 min of simulation. Note that the $\Delta C_2H_4/\Delta CO$ enhancement ratio is divided by a factor of 2.

In the plume from a savanna fire, a strong reduction of the enhancement ratio compared to CO of a number of compounds, including ethene and propene, have been found [*Hobbs et al.*, 2003].

[55] These observations support the simulation results showing a significant photochemical oxidation of alkenes in the plume on the timescale of hours. The reduction of the $\Delta C_2H_4/\Delta CO$ enhancement ratio observed in the Alaskan plume (reduction by ∼15%) is comparable to the simulated reduction of ∼16%. It can be concluded that oxidation of alkenes and therefore the oxidation capacity in the plume seems to be reasonably well described in the presented model simulation.

[56] Within a model, the oxidation efficiency can be derived as the inverse of the lifetime of hydrocarbons against oxidation by OH [*Lawrence et al.*, 2001]. From the model simulations, the lifetimes of hydrocarbons against oxidation by OH can be determined by dividing the total number of oxidized molecules by the number of emitted molecules. The resulting lifetimes of CO, C_2H_6, C_2H_4, and C_3H_6 are presented in Table 4.

[57] Compared to "typical lifetimes" [*Jenkin and Clemitshaw*, 2000], the lifetimes presented here are shorter, because the OH concentrations used in the general calculations are diurnally averaged values, which are generally lower than the instantaneous value used here. These lifetimes are useful quantitative indicators for the photochemical activity and will be used for a comparison of the different sensitivity simulations in the next sections.

[58] In the following, the main sources and sinks of the radicals will be investigated. For this purpose, the HO_x family is defined in order to exclude the fast chemical reactions involved in null cycles: HO_x = OH + HO_2 + CH_3O_2 + $C_2H_6O_2$ + EO_2 + EO + PO_2 + $CH_3COCH_2O_2$ + PA + GCO3 + HNO_4 + HONO + $CH_3O_2NO_2$ + PAN. Besides the radicals, some compounds of the NO_z family are also included. Under boundary layer conditions, these

compounds (e.g., PAN, HNO_4, HONO, and $CH_3O_2NO_2$) do not act as a permanent sink for the radicals.

[59] The photochemical production of the HO_x family, $P(HO_x)$, in the plume is dominated by the photolysis of formaldehyde, which accounts for 83.1% of the total HO_x production. Additional contributions come from the photolysis of acetaldehyde (7.9%), the reaction $O(^1D)$ + H_2O (4.7%), and the ozonolysis of propene (2.4%). On a global scale, the reaction of $O(^1D)$ with H_2O dominates the HO_x production [*Crutzen et al.*, 1999]. However, photolysis of HCHO and other aldehydes can be locally the most important source for HO_x radicals, e.g., under urban polluted conditions [*Jenkin and Clemitshaw*, 2000]. The photochemical loss of HO_x, $L(HO_x)$, under the conditions of a biomass-burning plume is dominated by the reaction of OH with NO_2 which accounts for 97.9% of the total HO_x loss. Because PAN is included in the HO_x family in the present investigation, its formation is no loss of HO_x. The self reaction of HO_2 and the reaction of HO_2 with CH_3O_2, which are significant in the global atmosphere, are only of minor importance under these conditions. No enhanced concentrations of hydroperoxides are found in the simulations.

[60] Direct emission of HCHO from the fire is the dominant source of this species. Secondary formation of formaldehyde due to the oxidation of hydrocarbons accounts for 12% of the total HCHO emission, the dominant reactions being CH_3O_2 + NO (33%), EO_2 + NO (11%), decomposition of EO (24%), and PO_2 + NO (28%). As for the photochemical ozone production presented in section 4.2.1, the important role of the alkenes for the photochemistry in young biomass-burning plumes is also reflected in their large contribution to secondary HCHO formation. The importance of the alkene oxidation for the photochemical production of ozone and the formation of HCHO has recently been found also for plumes from petrochemical facilities [*Wert et al.*, 2003].

5. Sensitivity Studies

[61] In this section, three sensitivity studies are presented and their results are compared to the results from the reference simulation.

[62] In the NO OVOC model simulation, the emissions of oxygenated volatile organic compounds (OVOC), i.e., HCHO, CH_3CHO, CH_3OH, HCOOH, CH_3COOH, and CH_3COCH_3, have been omitted. A recent box model study already showed the importance of the oxygenated compounds and their complex effects on ozone production in a biomass-burning plume [*Mason et al.*, 2001]. The LOW NOX scenario investigates the impact of a different $\Delta NO_x/\Delta CO_2$ emission ratio, which in actual fires depends strongly

Table 4. Simulated Lifetime of CO, C_2H_6, C_2H_4, and C_3H_6 Against Reaction With OH

Compound	Lifetime
CO	16.8[a]
C_2H_6	16.4[a]
C_2H_4	13.4[b]
C_3H_6	4.4[b]

[a]In days.
[b]In hours.

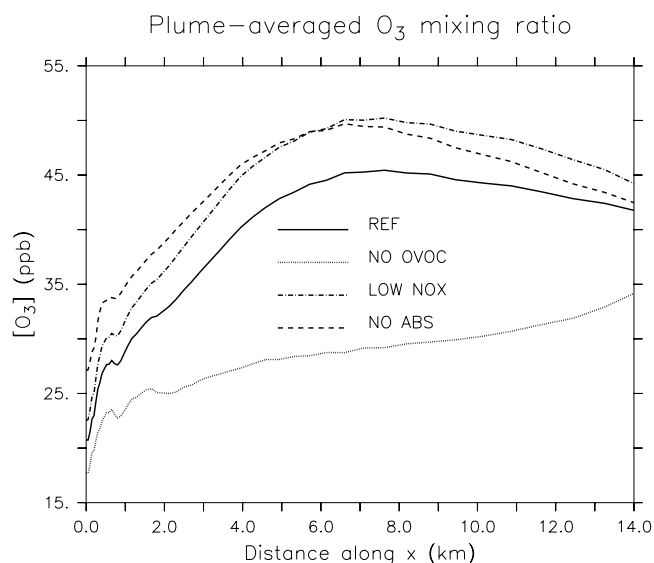**Figure 8.** Plume-averaged O_3 mixing ratios for the reference and the sensitivity simulations with distance from the plume.

Table 5. Averaged and Maximum Value for the O_3 Mixing Ratio From the Four Simulations[a]

	$[O_3]_{ave}$, ppb	$[O_3]_{max}$, ppb	$P(O_x)_{ave}$, molecule cm^{-3} s^{-1}	$P(O_x)_{tot}$, molecule
REF	39.4	70.4	1.84×10^8	5.67×10^{27}
NO OVOC	28.0	59.1	2.70×10^7	7.52×10^{26}
LOW NOX	43.4	91.4	2.01×10^8	6.13×10^{27}
NO ABS	43.6	92.3	2.40×10^8	7.51×10^{27}

[a]Additionally, the plume-averaged O_x production rate and the total number of O_x produced within 90 min of the simulation are shown.

simulations, the photochemical ozone production is larger than in the REF simulation, leading to ~10% higher ozone concentrations.

[66] From this analysis, the following can be concluded: The emissions of OVOCs have a significant impact on the simulation of the ozone concentration in a young biomass-burning plume. Neglecting their emission leads to unrealistically low ozone concentrations due to an underestimation of the photochemical ozone production. Reduced NO_x emissions in this scenario lead to an increased photochemical O_x production and ozone concentrations. The absorbing properties of the aerosol have a substantial effect on the simulated ozone concentration, leading to enhanced concentrations for the case of a nonabsorbing aerosol. Especially close to the fire, at high aerosol and NO_x concentrations, multiple scattering enhances photolysis frequencies, photochemical ozone production, and ozone concentrations.

5.2. Nitrogen Species

[67] The plume-averaged mixing ratios of the NO_z compounds along the distance from the fire for all four simulations are displayed in Figure 9. In the NO OVOC simulation only a small enhancement of NO_z compared to the background is observed downwind of the fire. The highest NO_z mixing ratio is observed in the NO ABS simulation, with a maximum value inside the plume of 24.4 ppb. The increase of the NO_z concentration inside of the plume begins much closer to the fire in the NO ABS
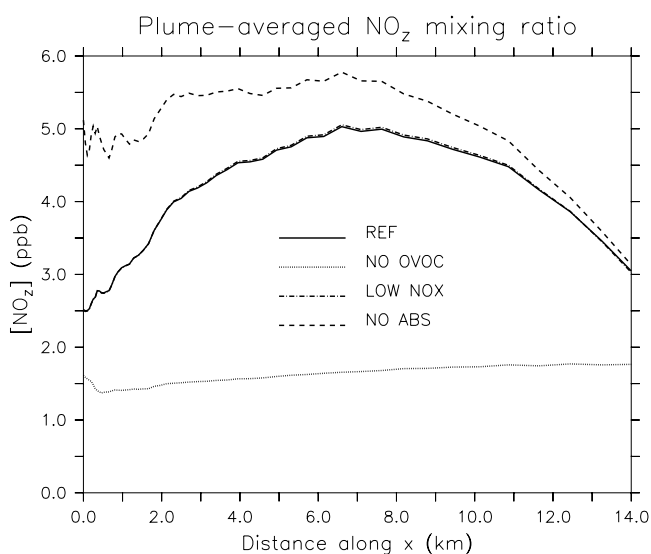
on the fuel nitrogen content and the phase of the fire. For the LOW NOX simulation, the $\Delta NO_x/\Delta CO_2$ emission ratio was reduced from 0.2% used in the REF simulation to 0.15%. The NO ABS scenario investigates the impact of aerosol absorption on the photochemical processes in a biomass-burning plume. In the NO ABS simulation, the single-scattering albedo of the aerosol was set to unity at all wavelengths, resulting in a radiatively conservative, nonabsorbing aerosol.

[63] In the following sections, the results of the simulation of ozone, nitrogen oxides, and the oxidation efficiency from the different simulations will be shown and discussed.

5.1. Ozone

[64] Figure 8 displays the plume-averaged ozone mixing ratios for the reference run and the three sensitivity studies. In the NO OVOC simulation, the simulated ozone concentration in the plume stays below background level at all distances from the fire, although a slight increase with distance from the fire is simulated. The ozone concentration of the LOW NOX and NO ABS simulations show highly elevated ozone concentrations inside the plume as compared to the background. The ozone mixing ratios also exceed the results from the REF simulation. The NO OVOC simulation lies well below all other model runs while the results from the NO ABS and LOW NOX simulations exceed the reference simulation at all distances from the fire. Close to the fire, the NO ABS simulation results in the highest averaged ozone concentration whereas downwind of 6 km the LOW NOX scenario simulates the highest ozone values.

[65] The results of the different simulations for ozone are summarized in Table 5. Here, the maximum and the plume-averaged ozone mixing ratios, the average O_x production rate, as well as the total number of photochemically produced O_x molecules are presented. In the NO OVOC simulation, $P(O_x)_{ave}$ is nearly an order of magnitude smaller than in the other simulations, resulting in a ~30% smaller ozone concentration. In the LOW NOX and NO ABS

Figure 9. Same as Figure 8 but for NO_z.

Table 6. Average and Maximum Value for the NO_z Mixing Ratio From the Four Simulations[a]

	[NO_z]$_{ave}$, ppb	[NO_z]$_{max}$, ppb	$P(NO_z)$, molecule cm^{-3} s^{-1}	$P(HNO_3)$, % of $P(NO_z)$	$\tau(NO_x)$, h
REF	4.2	19.3	2.82×10^7	61.0	9.9
NO OVOC	1.6	3.2	5.06×10^6	84.3	19.8
LOW NOX	4.2	19.8	2.83×10^7	56.1	9.5
NO ABS	5.0	24.4	3.58×10^7	60.1	7.7

[a]Additionally, the average rates of the net production of NO_z in the plume, $P(NO_z)$, during the 90 min of simulation are shown. The contribution of the net production of HNO_3, $P(HNO_3)$, to $P(NO_z)$ and the lifetime of NO_x against formation of HNO_3 and PAN are presented.

than in all other simulations. The NO_z mixing ratios calculated in the LOW NOX and the REF simulations show very close agreement; the values from the LOW NOX simulations slightly exceed the REF simulation.

[68] The results for the nitrogen reservoir species are summarized in Table 6. The maximum and the average NO_z mixing ratios are presented, reflecting the results shown in Figure 9 with low values in the NO OVOC simulation and the highest values in the NO ABS simulation. The same trend is reflected in the photochemical production of NO_z, $P(NO_z)$. Note, that $P(NO_z)$ denotes the net production of NO_z. The relative contribution of $P(HNO_3)$ to $P(NO_z)$ differs between the scenarios. The highest relative contribution of HNO_3 is simulated in the NO OVOC calculation, however the total amount of NO_z is very small.

[69] The partitioning of NO_z in the REF and NO ABS simulation is similar, although the absolute value of NO_z differs by roughly 20%. In the case of the LOW NOX simulation, the mixing ratio of NO_z is close to that of the REF simulation, but the contribution of HNO_3 is lower. The photochemical lifetime of NO_x against formation of HNO_3 and PAN is strongly enhanced when OVOC emissions from the fire are neglected. Lower NO_x emission and higher photolysis frequencies lead to a slight reduction in the photochemical lifetime of NO_x.

5.3. Oxidizing Efficiency

[70] In Figure 10, the plume-averaged OH mixing ratios are displayed for all four simulations as a function of distance. The OH concentration in the NO OVOC simulation is significantly lower than that in all other simulations. The results from the NO ABS and the LOW NOX simulation exceed the REF simulation. The average OH mixing ratio from the LOW NOX simulation follows the REF simulation along the plume at a higher level. The NO ABS simulation is significantly larger close to the fire and decreases to the value of the REF simulation at a distance of 14 km from the fire.

[71] In Tables 7 and 8, the relevant results from the four simulations for the oxidation efficiency of the plume are given. The plume-averaged OH concentrations in the LOW NOX and NO ABS are only slightly higher than in the REF simulation, ~12%. However, in the NO OVOC scenario, the average OH concentrations are significantly lower than in the REF scenario.

[72] The largest maximum OH and HO_2 mixing ratios are simulated in the NO ABS simulation, close to the fire.

However, the largest averaged HO_2 mixing ratio is simulated by the LOW NOX scenario. The averaged photochemical production rate of HO_x is nearly identical in the REF and LOW NOX simulation, while it is much smaller in the NO OVOC simulation. The highest value of $P(HO_x)$ is found in the NO ABS simulation. In all cases, the photolysis of HCHO is the main individual source of HO_x, with a contribution of more than 80% in the scenarios that include primary HCHO emission. Even in the NO OVOC scenario, where primary HCHO emissions are neglected, HCHO photolysis accounts for 46% of the HO_x production. The second most important reaction in this scenario is the reaction of $O(^1D)$ with H_2O, which accounts for 30% of the HO_x production rate. In the last column of Table 8, the lifetimes of propene under the different scenarios are presented. Although the average OH concentration is the same, the calculated propene lifetimes differ significantly between the LOW NOX and the NO ABS simulations.

5.4. Discussion

[73] From the results presented, the following conclusions concerning the photochemical processes occurring in a young biomass-burning plume can be derived.

[74] Plume chemistry is strongly dominated by the direct emission of trace gases and aerosol particles from the fire. Owing to the extremely high concentration of nitrogen oxides, photochemical production of ozone occurs in all investigated scenarios. However, the absolute amount of ozone produced and the resulting ozone concentration strongly depend on the fire emissions and the optical properties of the emitted aerosol. In all presented scenarios, radical loss occurs almost exclusively via the reaction of OH with NO_2. The reactions between radicals, e.g., the self reaction of HO_2, are only of very minor importance. This dominance of the radical loss via NO_2 is an indication that ozone production occurs in the hydrocarbon limited regime [*Kleinman et al.*, 1997]. The VOC sensitivity of the ozone production in a biomass-burning plume during the first hours was also found in a box model study [*Mason et al.*, 2001].
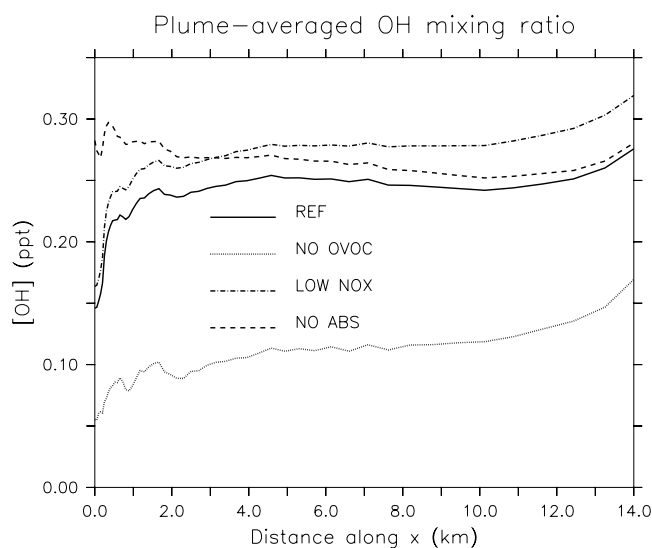

Figure 10. Same as Figure 8 but for OH.

Table 7. Average and Maximum Value for the OH and HO_2 Mixing Ratios From the Four Simulations After 90 min

	$[OH]_{ave}$, $[OH]_{max}$, ppt	$[HO_2]_{ave}$, $[HO_2]_{max}$, ppt
REF	0.24, 0.83	4.92, 12.32
NO OVOC	0.11, 1.04	1.24, 10.58
LOW NOX	0.27, 0.77	7.67, 15.75
NO ABS	0.27, 1.30	5.55, 18.41

[75] Neglect of the primary emission of OVOCs from the fire leads to significant changes in photochemistry, resulting in ozone concentrations in the plume that are significantly lower than observed. Ozone production in the NO OVOC simulation is limited by the availability of peroxy radicals. Their average concentrations are extremely low compared to the REF simulation (Table 7), because emission of HCHO, which serves as the dominant precursor for radicals in the plume, is not taken into account. However, even without primary HCHO emission, the photolysis of HCHO is the largest single source of radicals, because HCHO is secondarily produced from the oxidations of hydrocarbons. The reduced concentrations of radicals are also responsible for the relatively small formation of NO_z compounds in the NO OVOC simulation, and the increased lifetime of NO_x (Table 6) as well as the long lifetime of propene, representing a low oxidation efficiency. The enhanced contribution of HNO_3 to the concentration of NO_z as compared to the other simulations is explained by the neglect of the emissions of acetaldehyde, which is the main precursor of PAN.

[76] A reduction of the NO_x emission leads to enhanced photochemical ozone production through reactions of NO with peroxy radicals. The lower NO concentration in the LOW NOX scenario is counteracted by enhanced radical concentrations (Table 7), because of a reduced radical loss. Additionally, the partitioning between OH and the peroxy radicals changes under lower NO_x mixing ratios, leading to a larger contribution of the peroxy radicals to the total radical concentration. Lower NO_x mixing ratios reduce the loss of OH through formation of HNO_3, although the OH mixing ratio slightly increases. The higher concentration of peroxy radicals, especially that of the peroxyacetyl radical (PA), can compensate for the reduced NO_x concentration leading to enhanced formation of PAN as compared to HNO_3 (Table 6). This effect was also observed in the model study by *Mason et al.* [2001]. The oxidation efficiency is enhanced in the LOW NOX simulation as compared to the REF case. This can be seen in the lifetime of propene (Table 8). The decrease in $\tau(C_3H_6)$ is of the same order of magnitude as the increase of the average OH concentration ($\sim$10%).

[77] The change in the absorbing properties of the emitted aerosol particles has the largest effect on atmospheric photochemistry for the sensitivity studies considered here. Owing to enhanced photolysis in the plume, especially that of HCHO, radical production is highly enhanced. Especially close to the fire, the OH mixing ratio from the NO ABS simulation exceeds the results from the other scenarios (Figure 10), because in this region the concentrations of the main HO_x precursor, HCHO, and the aerosol particles are highest. Photochemical ozone production for this scenario is highly enhanced compared to the other studies.

[78] The total amount of photochemically produced NO_z is also highest in the NO ABS simulation, although the average concentrations of OH and HO_2 are smaller or identical to the LOW NOX simulation. However, high radical concentrations are present in the NO ABS simulations close to the fire (Figure 10 for OH) where the NO_x concentration is largest also. In this region, most of the NO_z production occurs in the NO ABS case, leading to highly elevated NO_z concentrations in this simulation close to the fire (Figure 9). The misleading character of the plume-averaged OH mixing ratio is also seen in the comparison of the propene lifetime between the LOW NOX and the NO ABS simulations. Although the averaged OH mixing ratio is identical in both scenarios, the propene lifetime differs by $\sim$18%. The reason for the shorter lifetime in the NO ABS simulation are the different spatial distributions of the OH concentration in the two scenarios. While in the LOW NOX case, the highest average value is found in the downwind part of the plume, the OH mixing ratio in the NO ABS simulation maximizes above the fire (Figure 10). As the removal of propene is much more effective close to the fire, because of its high concentration, the lifetime of propene is shorter in the NO ABS scenario. A similar problem exists when mean OH concentrations from global models are compared [*Lawrence et al.*, 2001].

6. Conclusions

[79] In the present study, the photochemical processes in a young biomass-burning plume were investigated with a three-dimensional chemical transport model. Meteorological conditions were taken from a previous simulation representing the situation of the plume from the Quinault prescribed fire. A chemical mechanism describing the oxidation of volatile organic compounds (VOCs) for the use in 3-D atmospheric transport models under the conditions of a biomass-burning plume was presented. The modeled concentrations of CO and other primary emissions are in the range of observations.

[80] Close to the fire, ozone in the plume is highly depleted compared to background concentrations, due to the reaction of ozone with the emitted NO. Photochemical ozone production occurs in the plume at a rate of $\sim$25 ppb h^{-1} and the downwind ozone concentration increases well above the background level. The simulated maximum value of 70 ppb ozone is reasonably close to observations in the plume from the Quinault fire and from other biomass-burning plumes. Photochemical ozone production is dominated by the reaction of HO_2 with NO ($\sim$69%). Peroxy radicals from the alkenes also contribute significantly to ozone production. Formation of nitrogen reservoir species, NO_z, is dominated by HNO_3, which

Table 8. Average HO_x Production Rates in the Plume as Well as the Relative Contribution of HCHO Photolysis are Presented

	$P(HO_x)$, molecule cm^{-3} s^{-1}	$J(HCHO)$, % of $P(HO_x)$	$\tau(C_3H_6)$,[a] h
REF	2.80×10^7	83.1	4.4
NO OVOC	3.74×10^6	46.4	19.8
LOW NOX	2.82×10^7	82.6	4.0
NO ABS	3.55×10^7	83.9	3.3

[a]Calculated lifetime of propene.

accounts for ~60% of the NO_z production. Significant atmospheric oxidation of alkenes occurs within the first tens of minutes after their release into the atmosphere. Photochemistry in biomass-burning plumes is limited by the availability of radicals. Their photochemical production occurs mainly from the photolysis of formaldehyde, which is emitted from the fire. Secondary production from the oxidation of VOCs accounts for ~12% of the HCHO concentration.

[81] In three sensitivity studies, the importance of the oxygenated volatile organic compounds (OVOCs), the emission ratio of NO_x, and the light-absorbing properties of the aerosol for the simulation of the ozone concentration were shown. The neglect of the primary emissions of OVOCs leads to unrealistically low ozone concentrations. A reduced emission ratio of NO_x or the specification of a nonabsorbing aerosol enhance the predicted ozone concentration. The production of radicals through the photolysis of HCHO is crucially important for the formation of ozone and nitrogen reservoir species, and the oxidation of alkenes. Any change in this source of radicals, e.g., through the neglect of primary HCHO emissions or through enhanced photolysis due to less aerosol absorption, has a significant effect on photochemistry. Enhanced radical production leads to enhanced ozone production, enhanced formation of nitrogen reservoir species, and a higher oxidation efficiency. The oxidation efficiency in the plume is not only linked to the average concentration of the OH radical, but additionally to the spatial distribution of its concentration. The decrease in the enhancement ratio between propene and CO is a good indicator for the oxidation efficiency in a biomass-burning plume.

[82] The results from this study show that ATHAM is a valuable tool to investigate photochemical processes in young biomass-burning plumes. Future studies will focus on the simulation of vegetation fires in different regions, e.g., the boreal forest, and the tropical savanna. The potential formation of a convective cloud from the fire-induced convection allows the investigation of several other atmospheric processes, e.g., scavenging of gas phase species into water droplets and ice particles, aerosol-cloud interaction, and the formation of ice. As ATHAM includes all the required modules, it is an excellent tool for further studies on the atmospheric processes in young biomass-burning plumes.

References

Andreae, M. O., and P. Merlet, Emission of trace gases and aerosols from biomass burning, *Global Biogeochem. Cycles*, *15*, 955–966, 2001.

Andreae, M. O., et al., Biomass-burning emissions and associated haze layers over Amazonia, *J. Geophys. Res.*, *93*, 1509–1527, 1988.

Andreae, M. O., B. E. Anderson, D. R. Blake, J. D. Bradshaw, J. E. Collins, G. L. Gregory, G. W. Sachse, and M. C. Shipham, Influence of plumes from biomass burning on atmospheric chemistry over the equatorial and tropical South Atlantic during CITE 3, *J. Geophys. Res.*, *99*, 12,793–12,808, 1994.

Andreae, M. O., J. Fishman, and J. Lindesay, The Southern Tropical Atlantic Region Experiment (STARE): Transport and Atmospheric Chemistry near the Equator-Atlantic (TRACE A) and Southern African Fire-Atmosphere Research Initiative (SAFARI): An introduction, *J. Geophys. Res.*, *101*, 23,519–23,520, 1996a.

Andreae, M. O., et al., Methyl halide emissions from savanna fires in southern Africa, *J. Geophys. Res.*, *101*, 23,603–23,613, 1996b.

Andreae, M. O., et al., Transport of biomass burning smoke to the upper troposphere by deep convection in the equatorial region, *Geophys. Res. Lett.*, *28*, 951–954, 2001.

Cahalan, R. F., W. Rodgway, W. J. Wiscombe, T. L. Bell, and J. B. Snider, The albedo of fractal stratocumulus clouds, *J. Atmos. Sci.*, *51*, 2434–2455, 1994.

Chandra, S., J. R. Ziemke, P. K. Bhartia, and R. V. Martin, Tropical tropospheric ozone: Implications for dynamics and biomass burning, *J. Geophys. Res.*, *107*(D14), 4188, doi:10.1029/2001JD000447, 2002.

Chatfield, R. B., and A. C. Delany, Convection links biomass burning to increased tropical ozone, however, models will typically over-predict O_3, *J. Geophys. Res.*, *95*, 18,473–18,488, 1990.

Crutzen, P. J., and M. O. Andreae, Biomass burning in the tropics: Impact on atmospheric chemistry and biogeochemical cycles, *Science*, *250*, 1669–1678, 1990.

Crutzen, P. J., M. G. Lawrence, and U. Pöschl, On the background photochemistry of tropospheric ozone, *Tellus, Ser. B*, *51*, 123–146, 1999.

Damian, V., A. Sandu, M. Damian, F. Potra, and G. R. Carmichael, The Kinetic PreProcessor KPP—A software environment for solving chemical kinetics, *Comput. Chem. Eng.*, *26*, 1567–1579, 2002.

Delmas, R., J. P. Lacaux, J. C. Menaut, L. Abbadie, X. Le Roux, G. Helas, and J. Lobert, Nitrogen compound emission from biomass burning in tropical African savanna FOS/DECAFE 1991 experiment (Lamto, Ivory Coast), *J. Atmos. Chem.*, *22*, 175–193, 1995.

Delmas, R. A., et al., Experiment for Regional Sources and Sinks of Oxidants (EXPRESSO): An overview, *J. Geophys. Res.*, *104*, 30,609–30,624, 1999.

Evans, L. F., I. A. Weeks, A. J. Eccleston, and D. R. Packham, Photochemical ozone in smoke from prescribed burning of forests, *Environ. Sci. Technol.*, *11*, 896–900, 1977.

Ferek, R. J., J. S. Reid, P. V. Hobbs, D. R. Blake, and C. Liousse, Emission factors of hydrocarbons, halocarbons, trace gases and particles from biomass burning in Brazil, *J. Geophys. Res.*, *103*, 32,107–32,118, 1998.

Ferguson, S. A., D. V. Sandberg, and R. Ottmar, Modelling the effects of landuse changes on global biomass emissions, in *Biomass Burning and Its Inter-relationships With the Climate System*, edited by J. L. Innes, M. Beniston, and M. M. Verstraete, pp. 33–50, Kluwer Acad., Norwell, Mass., 2000.

Fishman, J., and V. G. Brackett, The climatological distribution of tropospheric ozone derived from satellite measurements using version 7 Total Ozone Mapping Spectrometer and Stratospheric Aerosol and Gas Experiment data sets, *J. Geophys. Res.*, *102*, 19,275–19,278, 1997.

Fishman, J., K. Fakhruzzaman, B. Cros, and D. Nganga, Identification of widespread pollution in the Southern Hemisphere deduced from satellite analyses, *Science*, *252*, 1693–1696, 1991.

Galanter, M., H. Levy II, and G. R. Carmichael, Impacts of biomass burning on tropospheric CO, NO_x, and O_3, *J. Geophys. Res.*, *105*, 6633–6653, 2000.

Gassó, S., and D. A. Hegg, Comparison of columnar aerosol optical properties measured by the MODIS Airborne Simulator with *in situ* measurements: A case study, *Remote Sens. Environ.*, *66*, 138–152, 1998.

Goode, J. G., R. J. Yokelson, R. A. Susott, and D. E. Ward, Trace gas emissions from laboratory biomass fires measured by open-path Fourier transform infrared spectroscopy: Fires in grass and surface fuels, *J. Geophys. Res.*, *104*, 21,237–21,245, 1999.

Goode, J. G., R. J. Yokelson, D. E. Ward, R. A. Susott, R. E. Babbitt, M. A. Davis, and W. M. Hao, Measurements of excess O_3, CO_2, CH_4, C_2H_4, C_2H_2, HCN, NO, NH_3, HCOOH, CH_3COOH, HCHO, and CH_3H in 1997 Alaskan biomass burning plumes by airborne Fourier transform infrared spectroscopy (AFTIR), *J. Geophys. Res.*, *105*, 22,147–22,166, 2000.

Graf, H.-F., M. Herzog, J. M. Oberhuber, and C. Textor, Effect of environmental conditions on volcanic plume rise, *J. Geophys. Res.*, *104*, 24,309–24,320, 1999.

Granier, C., J.-F. Müller, and G. Brasseur, The impact of biomass burning on the global budget of ozone and ozone precursors, in *Biomass Burning and Its Inter-relationship With the Climate System*, edited by J. L. Innes, M. Beniston, and M. M. Verstraete, pp. 69–85, Kluwer Acad., Norwell, Mass., 2000.

Griffith, D. W., W. G. Mankin, M. T. Coeffey, D. E. Ward, and A. Riebau, FTIR remote sensing of biomass burning emissions of CO_2, CO, CH_4,

CH$_2$O, NO, NO$_2$, NH$_3$, and N$_2$O, in *Global Biomass Burning: Atmospheric, Climatic, and Biospheric Implications*, edited by J. S. Levine, pp. 230–239, MIT Press, Cambridge, Mass., 1991.

Harriss, R. C., S. C. Wofsy, J. M. Hoell Jr., R. J. Bendura, J. W. Drewry, R. J. McNeal, D. Pierce, V. Rabine, and R. L. Snell, The Arctic Boundary Layer Expedition (ABLE 3B): July–August 1990, *J. Geophys. Res.*, *99*, 1635–1643, 1994.

Helas, G., et al., Ozone production due to emissions from vegetation burning, *J. Atmos. Chem.*, *22*, 163–174, 1995.

Herzog, M., H.-F. Graf, C. Textor, and J. M. Oberhuber, The effect of phase changes of water on the development of volcanic plumes, *J. Volcanol. Geotherm. Res*, *87*, 55–74, 1998.

Hobbs, P. V., J. S. Reid, J. A. Herring, J. D. Nance, R. E. Weiss, J. L. Ross, D. A. Hegg, R. D. Ottmar, and C. Liousse, Particle and trace-gas measurements in the smoke from prescribed burns of forest products in the Pacific Northwest, in *Biomass Burning and Global Change*, edited by J. S. Levine, pp. 697–715, MIT Press, Cambridge, Mass., 1996.

Hobbs, P. V., P. Sinha, R. J. Yokelson, T. J. Christian, D. R. Blake, S. Gao, T. W. Kirchstetter, T. Novakov, and P. Pilewskie, Evolution of gases and particles from a savanna fire in South Africa, *J. Geophys. Res.*, *108*(D13), 8485, doi:10.1029/2002JD002352, 2003.

Holzinger, R., C. Warneke, A. Hansel, A. Jordan, W. Lindinger, D. H. Scharffe, G. Schade, and P. J. Crutzen, Biomass burning as a source of formaldehyde, acetaldehyde, methanol, acetone, acetonitrile, and hydrogen cyanide, *Geophys. Res. Lett.*, *26*, 1161–1164, 1999.

Jacob, D. J., et al., Summertime photochemistry of the troposphere at high northern latitudes, *J. Geophys. Res.*, *97*, 16,421–16,431, 1992.

Jenkin, M. E., and K. C. Clemitshaw, Ozone and other secondary photochemical pollutants: Chemical processes governing their formation in the planetary boundary layer, *Atmos. Environ.*, *34*, 2499–2527, 2000.

Jost, C., J. Trentmann, D. Sprung, M. O. Andreae, J. B. McQuaid, and H. Barjat, Trace gas chemistry in a young biomass burning plume over Namibia: Observations and model simulations, *J. Geophys. Res.*, *108*(D13), 8482, doi:10.1029/2002JD002431, 2003.

Kaufman, Y. J., et al., Relationship between remotely sensed fire intensity and rate of emission of smoke: SCAR-C experiment, in *Biomass Burning and Global Change*, edited by J. S. Levine, pp. 685–696, MIT Press, Cambridge, Mass., 1996.

Kaufman, Y. J., et al., Smoke, Clouds, and Radiation-Brazil (SCAR-B) experiment, *J. Geophys. Res.*, *103*, 31,783–31,808, 1998.

Kirchner, F., and W. R. Stockwell, Effect of peroxy radical reactions on the predicted concentrations of ozone, nitrogenous compounds, and radicals, *J. Geophys. Res.*, *101*, 21,007–21,022, 1996.

Kleinman, L. I., P. H. Daum, J. H. Lee, L. J. Nunnermacker, S. R. Springston, L. Newmann, J. Weinstein-Lloyd, and S. Sillman, Dependence of ozone production on NO and hydrocarbons in the troposphere, *Geophys. Res. Lett.*, *24*, 2299–2302, 1997.

Koppmann, R., A. Khedim, J. Rudolph, D. Poppe, M. O. Andreae, G. Helas, M. Welling, and T. Zenker, Emissions of organic trace gases from savanna fires in southern Africa during the 1992 Southern African Fire Atmosphere Research Initiative and their impact on the formation of tropospheric ozone, *J. Geophys. Res.*, *102*, 18,879–18,888, 1997.

Landgraf, J., and P. Crutzen, An efficient method for online calculations of photolysis and heating rates, *J. Atmos. Sci.*, *55*, 863–878, 1998.

Lawrence, M. G., P. J. Crutzen, P. J. Rasch, B. E. Eaton, and N. M. Mahowald, A model for studies of tropospheric photochemistry: Description, global distributions, and evaluation, *J. Geophys. Res.*, *104*, 26,245–26,277, 1999.

Lawrence, M. G., P. Jöckel, and R. von Kuhlmann, What does the global mean OH concentration tell us?, *Atmos. Chem. Phys.*, *1*, 37–49, 2001.

LeBel, P. J., W. R. Cofer III, J. S. Levine, S. A. Vay, and P. D. Roberts, Nitric acid and ammonia emissions from a mid-latitude prescribed wetlands fire, *Geophys. Res. Lett.*, *15*, 792–795, 1988.

LeBel, P. J., S. A. Vay, and P. D. Roberts, Ammonia and nitric acid emissions from wetlands and boreal forest fires, in *Global Biomass Burning: Atmospheric, Climatic, and Biospheric Implications*, edited by J. S. Levine, pp. 225–229, MIT Press, Cambridge, Mass., 1991.

Lefer, B. L., et al., Enhancement of acidic gases in biomass burning impacted air masses over Canada, *J. Geophys. Res.*, *99*, 1721–1737, 1994.

Lelieveld, J., and F. J. Dentener, What controls tropospheric ozone?, *J. Geophys. Res.*, *105*, 3531–3551, 2000.

Liu, S. C., M. Trainer, F. C. Fehsenfeld, D. D. Parrish, E. J. Williams, D. W. Fahey, G. Hübler, and P. C. Murphy, Ozone production in the rural troposphere and the implications for regional and global ozone distribution, *J. Geophys. Res.*, *92*, 4191–4207, 1987.

Lobert, J., and J. Warnatz, Emissions from combustion process in vegetation, in *Fire in the Environment: The Ecological, Atmospheric, and Climatic Importance of Vegetation Fires*, edited by P. Crutzen and J. Goldammer, pp. 15–37, John Wiley, Hoboken, N. J., 1993.

Lobert, J. M., D. H. Scharffe, W.-M. Hao, T. A. Kuhlbusch, R. Seuwen, P. Warneck, and P. J. Crutzen, Experimental evaluation of biomass burning emissions: Nitrogen and carbon containing compounds, in *Global Biomass Burning: Atmospheric, Climatic, and Biospheric Implications*, edited by J. S. Levine, pp. 289–304, MIT Press, Cambridge, Mass., 1991.

Marion, T., P. E. Perros, R. Losno, and E. Steiner, Ozone production efficiency in savanna and forested areas during the EXPRESSO experiment, *J. Atmos. Chem.*, *38*, 3–30, 2001.

Martins, J. V., P. Artaxo, P. V. Hobbs, C. Liousse, H. Cachier, Y. Kaufman, and A. Plana-Fattori, Particle size distribution, elemental composition, carbon measurements, and optical properties of smoke from biomass burning in the Pacific Northwest of the United States, in *Biomass Burning and Global Change*, edited by J. S. Levine, pp. 716–732, MIT Press, Cambridge, Mass., 1996.

Marufu, L., F. Dentener, J. Lelieveld, M. O. Andreae, and G. Helas, Photochemistry of the African troposphere: Influence of biomass-burning emissions, *J. Geophys. Res.*, *105*, 14,513–14,530, 2000.

Mason, S. A., R. J. Field, R. J. Yokelson, M. A. Kochivar, M. R. Tinsley, D. E. Ward, and W. M. Hao, Complex effects arising in smoke plume simulations due to inclusion of direct emissions of oxygenated organic species from biomass combustion, *J. Geophys. Res.*, *106*, 12,527–12,539, 2001.

Mauzerall, D. L., D. J. Jacob, S.-M. Fan, J. D. Bradshaw, G. L. Gregory, G. W. Sachse, and D. R. Blake, Origin of tropospheric ozone at remote high northern latitudes in summer, *J. Geophys. Res.*, *101*, 4175–4188, 1996.

Mauzerall, D. L., J. A. Logan, D. J. Jacob, B. E. Anderson, D. R. Blake, J. D. Bradshaw, B. Heikes, G. W. Sachse, H. Singh, and B. Talbot, Photochemistry in biomass burning plumes and implications for tropospheric ozone over the tropical South Atlantic, *J. Geophys. Res.*, *103*, 8401–8423, 1998.

McKeen, S. A., G. Wotawa, D. D. Parrish, J. S. Holloway, M. P. Buhr, G. Hübler, F. C. Fehsenfeld, and J. F. Meagher, Ozone production from Canadian wildfires during June and July of 1995, *J. Geophys. Res.*, *107*(D14), 4192, doi:10.1029/2001JD000697, 2002.

Oberhuber, J. M., M. Herzog, H.-F. Graf, and K. Schwanke, Volcanic plume simulation on large scales, *J. Volcanol. Geotherm. Res.*, *87*, 29–53, 1998.

Orlando, J. J., G. S. Tyndall, M. Bilde, C. Ferronato, T. J. Wallington, L. Vereecken, and J. Peeters, Laboratory and theoretical study of the oxy radicals in the OH- and Cl-initiated oxidation of ethene, *J. Phys. Chem. A*, *102*, 8116–8123, 1998.

Parrish, D. D., J. S. Holloway, M. Trainer, P. C. Murphy, G. L. Forbes, and F. C. Fehsenfeld, Export of North American ozone pollution to the North Atlantic Ocean, *Science*, *259*, 1436–1439, 1993.

Peters, W., M. Krol, F. Dentener, A. Thompson, and J. Lelieveld, Chemistry-transport modeling of the satellite observed distribution of tropical tropospheric ozone, *Atmos. Chem. Phys.*, *2*, 103–120, 2002.

Poppe, D., R. Koppmann, and J. Rudolph, Ozone formation in biomass burning plumes: Influence of atmospheric dilution, *Geophys. Res. Lett.*, *25*, 3823–3826, 1998.

Reid, J. S., P. V. Hobbs, R. J. Ferek, D. R. Blake, J. V. Martins, M. R. Dunlap, and C. Liousse, Physical, chemical, and optical properties of regional hazes dominated by smoke in Brazil, *J. Geophys. Res.*, *103*, 32,059–32,080, 1998.

Ryerson, T. B., et al., Emissions lifetimes and ozone formation in power plant plumes, *J. Geophys. Res.*, *103*, 22,569–22,583, 1998.

Sandberg, D. V., and J. Peterson, A source strength model for prescribed fire in coniferous logging slash, paper presented at the 21st Annual Meeting, Pac. Northwest Int. Sect. of the Air Pollut. Control Assoc., Portland, Oreg., 12–14 Nov. 1984.

Singh, H. N., et al., Summertime distribution of PAN and other reactive nitrogen species in the northern high-latitude atmosphere of eastern Canada, *J. Geophys. Res.*, *99*, 1821–1835, 1994.

Smolarkiewicz, P. K., A fully multidimensional positive definite advection transport algorithm with small implicit diffusion, *J. Comput. Phys.*, *54*, 325–362, 1984.

Stith, J. L., L. F. Radke, and P. V. Hobbs, Particle emissions and the production of ozone and nitrogen oxides from the burning of forest slash, *Atmos. Environ.*, *15*, 73–82, 1981.

Tanré, D., Y. J. Kaufman, M. Herman, and S. Mattoo, Remote sensing of aerosol properties over oceans using the MODIS/EOS spectral radiances, *J. Geophys. Res.*, *102*, 16,971–16,988, 1997.

Textor, C., H.-F. Graf, M. Herzog, and J. M. Oberhuber, Injection of gases into the stratosphere by explosive volcanic eruptions, *J. Geophys. Res.*, *108*(D19), 4606, doi:10.1029/2002JD002987, 2003.

Thompson, A. M., J. C. Witte, R. D. Hudson, H. Guo, R. R. Herman, and M. Fujiwara, Tropical tropospheric ozone and biomass burning, *Science*, *291*, 2128–2132, 2001.

Trainer, M., D. D. Parrish, P. D. Goldan, J. Roberts, and F. C. Fehsenfeld, Review of observation-based analysis of the regional factors influencing ozone concentrations, *Atmos. Environ.*, *34*, 2045–2061, 2000.

Trentmann, J., M. O. Andreae, H.-F. Graf, P. V. Hobbs, R. D. Ottmar, and T. Trautmann, Simulation of a biomass-burning plume: Comparison of model results with observations, *J. Geophys. Res.*, *107*(D2), 4013, doi:10.1029/2001JD000410, 2002.

Trentmann, J., B. Früh, O. Boucher, T. Trautmann, and M. O. Andreae, Three-dimensional solar radiation effects on the actinic flux field in a biomass-burning plume, *J. Geophys. Res.*, *108*(D17), 4558, doi:10.1029/2003JD003422, 2003.

Verwer, J. G., E. J. Spee, J. G. Blom, and W. H. Hundsdorfer, A second order Rosenbrock method applied to photochemical dispersion problems, *SIAM J. Sci. Comput.*, *20*, 1456–1480, 1999.

von Kuhlmann, R., M. G. Lawrence, P. J. Crutzen, and P. J. Rasch, A model for studies of tropospheric ozone and nonmethane hydrocarbons: Model description and ozone results, *J. Geophys. Res.*, *108*(D9), 4294, doi:10.1029/2002JD002893, 2003.

Ward, D. E., R. A. Susott, J. B. Kauffman, R. E. Babbitt, D. L. Cummings, B. Dias, B. N. Holben, and Y. J. Kaufman, Smoke and fire characteristics for cerrado and deforestation burns in Brazil: Base-B experiment, *J. Geophys. Res.*, *97*, 14,601–14,619, 1992.

Wert, B. P., et al., Signatures of terminal alkene oxidation in airborne formaldehyde measurements during TexAQS 2000, *J. Geophys. Res.*, *108*(D3), 4104, doi:10.1029/2002JD002502, 2003.

Yokelson, R. J., D. W. T. Griffith, and D. E. Ward, Open-path Fourier transform infrared studies of large-scale laboratory biomass fires, *J. Geophys. Res.*, *101*, 21,067–21,080, 1996.

Yokelson, R. J., R. Susott, D. E. Ward, J. Reardon, and D. W. T. Griffith, Emissions from smoldering combustion of biomass measured by open-path Fourier transform infrared spectroscopy, *J. Geophys. Res.*, *102*, 18,865–18,877, 1997.

Yokelson, R. J., I. T. Bertschi, T. J. Christian, P. V. Hobbs, D. E. Ward, and W. M. Hao, Trace gas measurements in nascent, aged, and cloud-processed smoke from African savanna fires by airborne Fourier transform infrared spectroscopy (AFTIR), *J. Geophys. Res.*, *108*(D13), 8478, doi:10.1029/2002JD002322, 2003.

Zdunkowski, W. G., W.-G. Panhans, R. M. Welch, and G. J. Korb, A radiation scheme for circulation and climate models, *Beitr. Phys. Atmos.*, *55*, 215–238, 1982.

———————————

M. O. Andreae, Department of Biogeochemistry, Max Planck Institute for Chemistry, P.O. Box 3060, D-55020 Mainz, Germany. (andreae@mpch-mainz.mpg.de)

H.-F. Graf, Department of Geography, University of Cambridge, Downing Place, Cambridge CB2 3EN, UK. (hfg21@cam.ac.uk)

J. Trentmann, Department of Atmospheric Sciences, University of Washington, Box 351640, Seattle, WA 98195, USA. (jtrent@atmos.washington.edu)
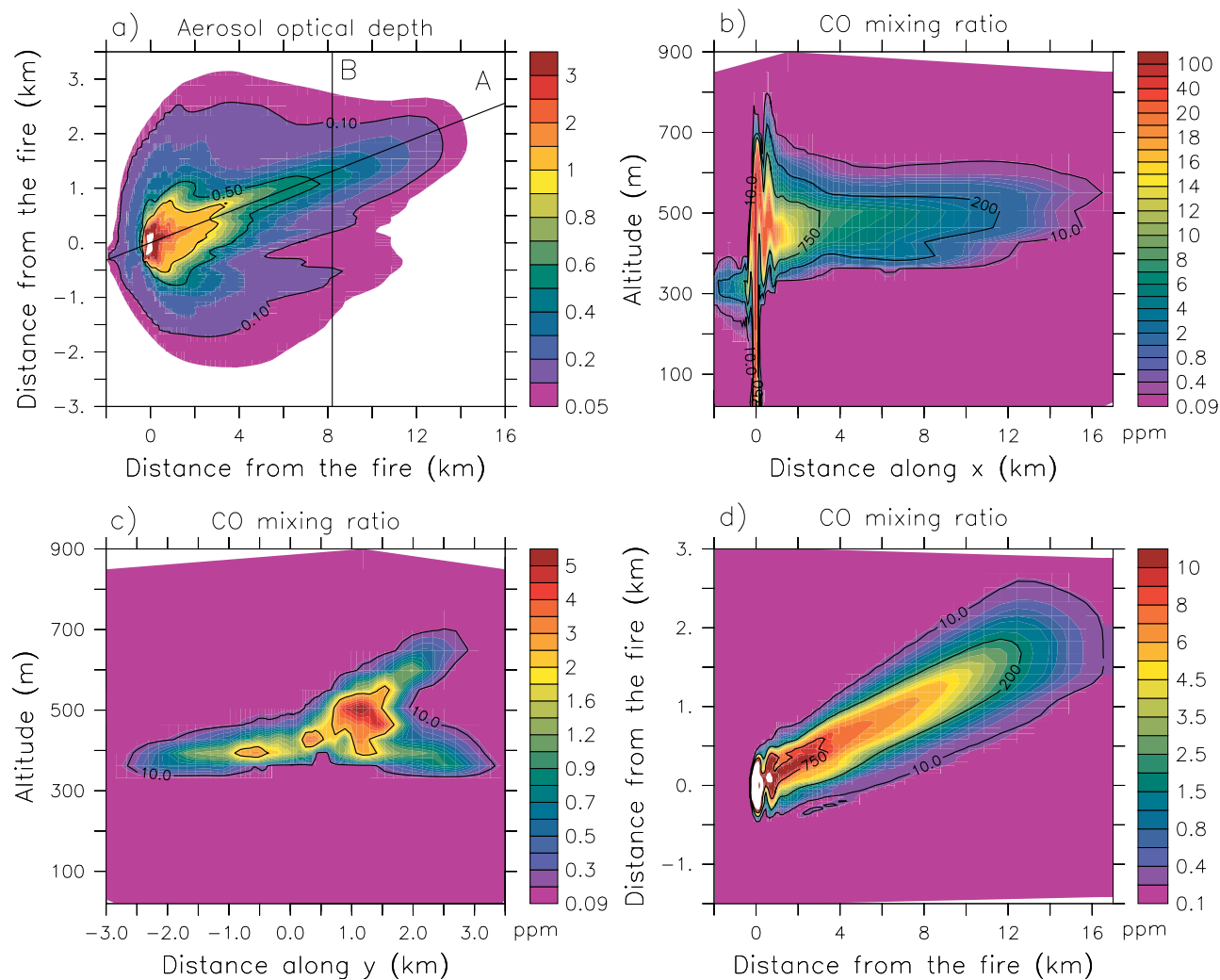
Figure 1. (a) Aerosol optical depth at 400 nm (color coding) after 90 min of simulation. The locations of the cross sections A and B are also shown. (b) CO mixing ratio (color coding) along the main plume axis, section A. (c) CO mixing ratio at section B across the plume at $x = 8.2$ km. (d) CO mixing ratio at an altitude of $z = 500$ m. Contour lines in Figures 1b–1d represent the aerosol mass concentration ($\mu g\ m^{-3}$). The white line indicates the border of the plume as defined by an aerosol mass concentration of $10\ \mu g\ m^{-3}$.
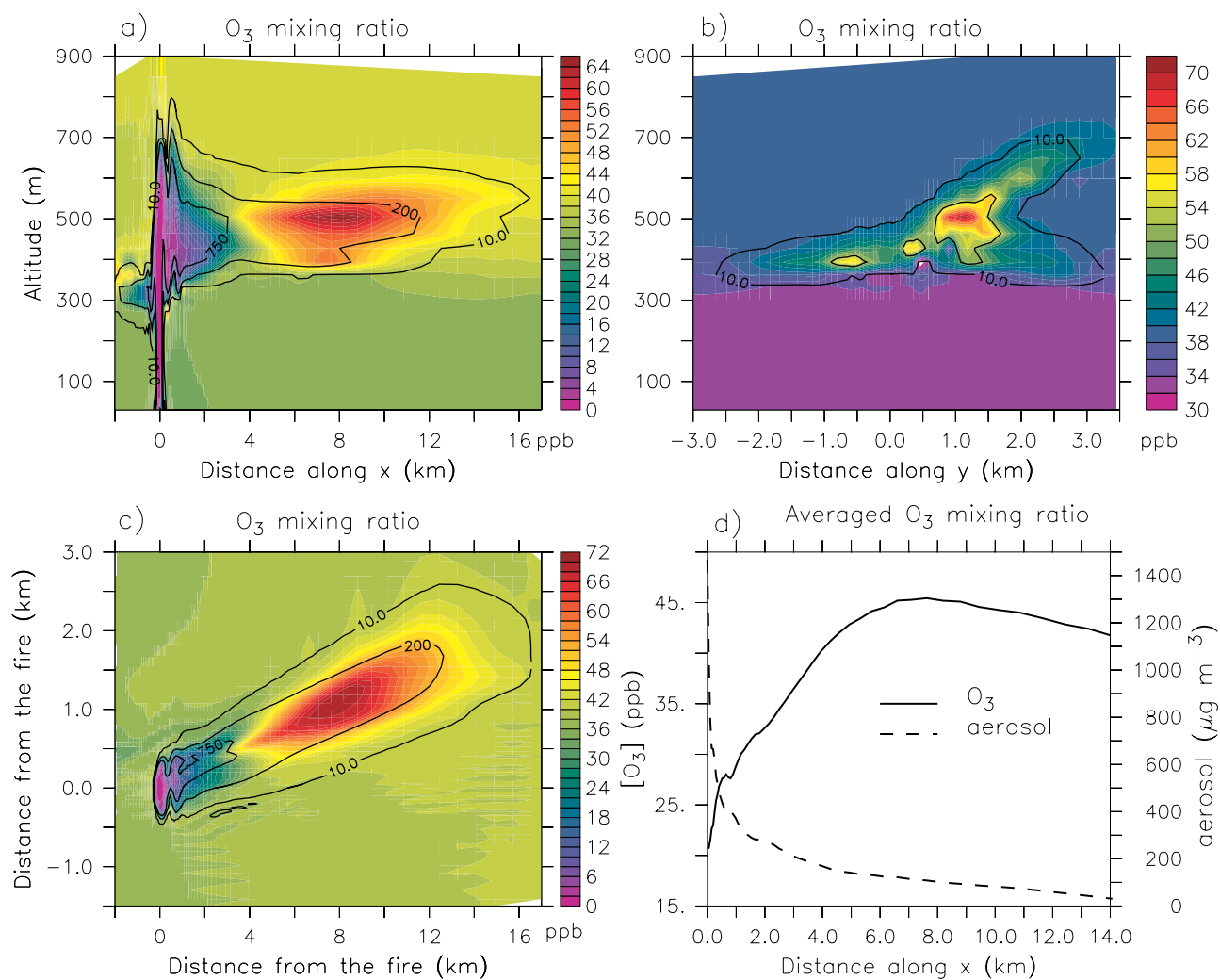
Figure 2. O_3 mixing ratio (color coding) for three cross sections through the model domain at (a) the main plume axis, section A in Figure 1a, (b) $x = 8.2$ km, section B in Figure 1a, and (c) $z = 500$ m after 90 min of simulation time. The traveling time from the source to the cross section at a distance of 8.2 km is ~40 min. Contour lines represent the aerosol mass concentration ($\mu g\ m^{-3}$). (d) Plume-averaged O_3 mixing ratio and aerosol mass concentration with distance from the fire.
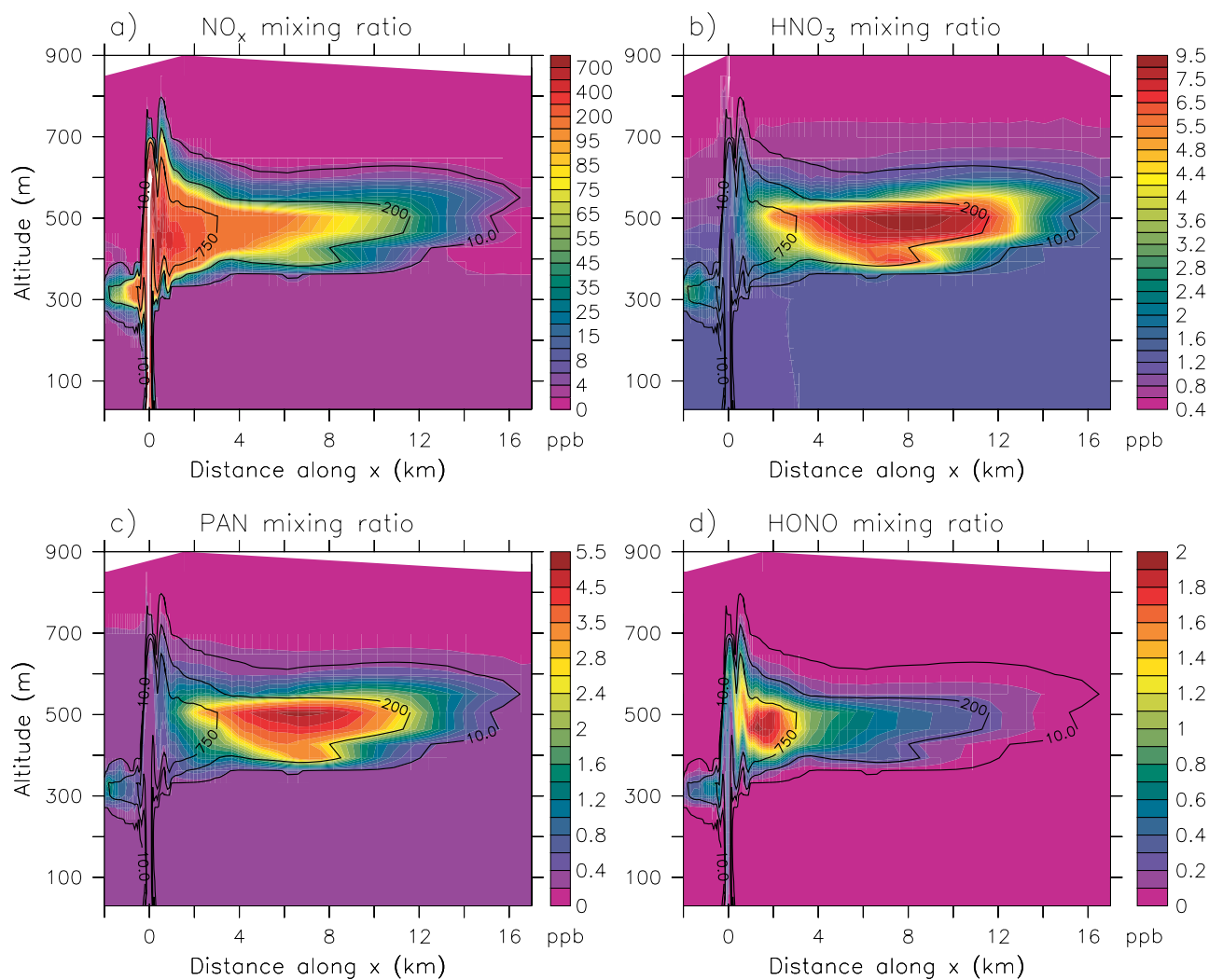
Figure 4. Mixing ratios of (a) NO_x and the most abundant NO_z species, i.e., (b) HNO_3, (c) PAN, and (d) HONO, along the main plume axis, section A in Figure 1a, after 90 min. Contour lines represent the aerosol mass concentration ($\mu g\ m^{-3}$).
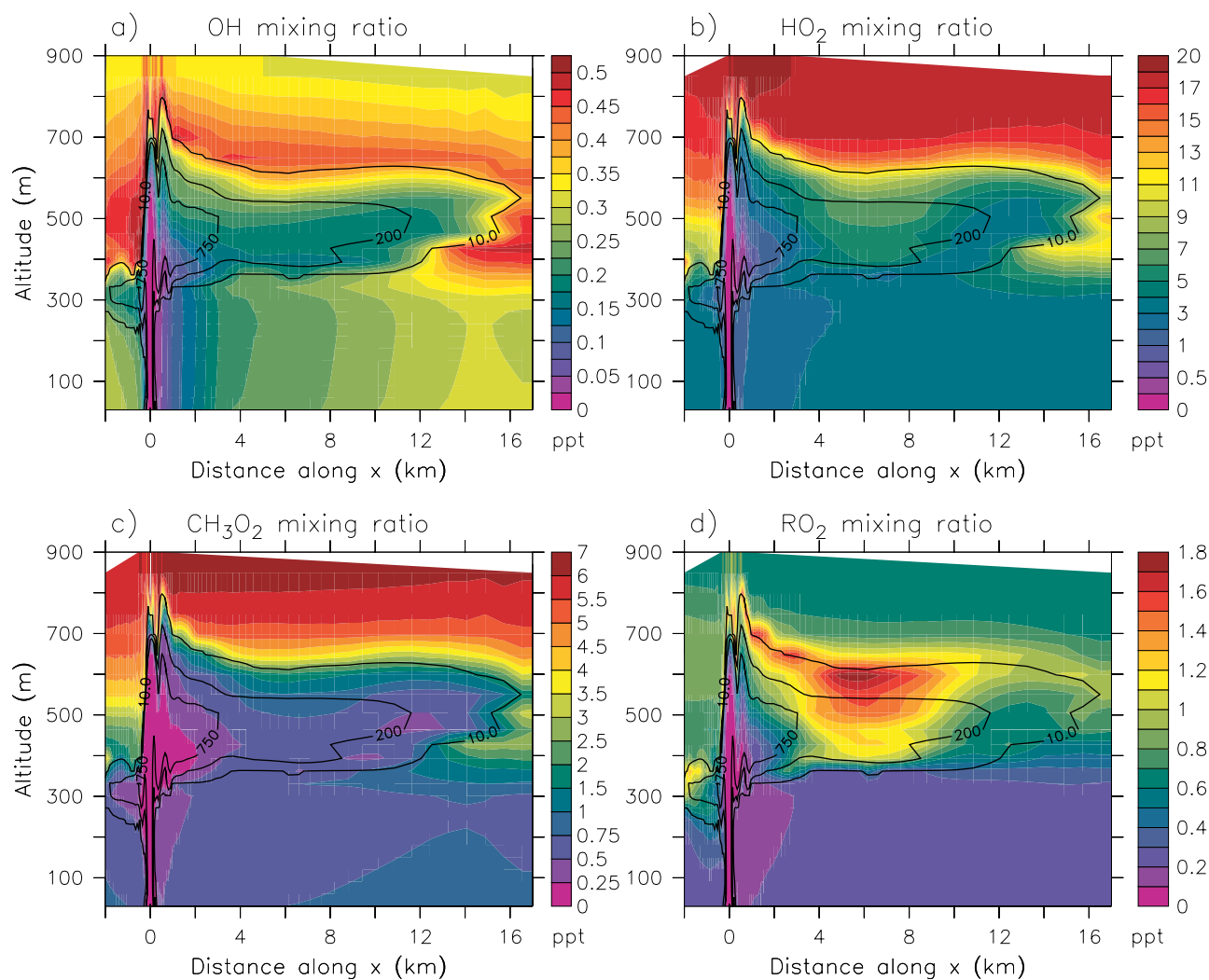
Figure 6. Simulated mixing ratios of (a) OH, (b) HO$_2$, (c) CH$_3$O$_2$, and (d) the sum of other peroxy radicals RO$_2$ (RO$_2$ = PA + C$_2$H$_6$O$_2$ + EO$_2$ + PO$_2$+ ACETO$_2$) after 90 min along the plume at y = 100 m. Contour lines represent the aerosol mass concentration (μg m^{-3}).